UNIVERSIDADE FEDERAL DO RIO DE JANEIRO

INSTITUTO DE FÍSICA

Associated production of $\Psi(2S)$ and Φ in diffractive proton-proton collisions at the LHCb experiment

Jeferson dos Santos Oliveira

M.Sc dissertation presented to the Graduate Program in Physics of the Institute of Physics of Universidade Federal do Rio de Janeiro – UFRJ, as part of the requirements to the obtention of the title of Master in Sciences (Physics).

Advisor: Murilo Santana Rangel
Co-advisor: Bruno Souza de Paula

Rio de Janeiro

2025

Associated production of $\Psi(2S)$ and Φ in diffractive proton-proton collisions at the LHCb experiment

Jeferson dos Santos Oliveira
Murilo Santana Rangel
Bruno Souza de Paula

Dissertação de Mestrado submetida ao Programa de Pós-Graduação em Física, Instituto de Física, da Universidade Federal do Rio de Janeiro – UFRJ, como parte dos requisitos necessários à obtenção do título de Mestre em Ciências (Física).

Aprovada por:

Prof. Dr. Murilo Santana Rangel, IF-UFRJ
(Presidente e Orientador)

Prof. Dr. Bruno Souza de Paula, IF-UFRJ
(Coorientador)

Prof. Dr. Rogerio Menezes de Almeida, IF-UFRJ

Profa. Dra. Helena Brandão Malbouisson, UERJ

Prof. Dr. Dilson de Jesus Damião, UERJ

Rio de Janeiro, 2025

CIP - Catalogação na Publicação

S237a

Santos Oliveira, Jeferson dos
Associated production of Psi(2S) and Phi in diffractive proton-proton collisions at the LHCb experiment / Jeferson dos Santos Oliveira. -- Rio de Janeiro, 2025.
88 f.

Orientador: Murilo Santana Rangel.
Coorientador: Bruno Souza de Paula.
Dissertação (mestrado) - Universidade Federal do Rio de Janeiro, Instituto de Física, Programa de Pós Graduação em Física, 2025.

1. Produção central exclusiva. 2. Difração. 3. Pomeron. 4. LHCb. 5. Física de altas energias. I. Santana Rangel, Murilo, orient. II. Souza de Paula, Bruno, coorient. III. Título.

Elaborado pelo Sistema de Geração Automática da UFRJ com os dados fornecidos pelo(a) autor(a), sob a responsabilidade de Miguel Romeu Amorim Neto - CRB-7/6283.

Resumo

Produção associada do $\psi(2S)$ e ϕ no regime difrativo em colisões proton-proton no experimento LHCb

Jeferson dos Santos Oliveira

Orientador: Murilo Santana Rangel

Coorientador: Bruno Souza de Paula

Resumo da Dissertação de mestrado apresentada ao Programa de Pós-Graduação em Física do Instituto de Física da Universidade Federal do Rio de Janeiro - UFRJ, como parte dos requisitos necessários à obtenção do título de Mestre em Ciências (Física).

Esse trabalho apresenta o primeiro estudo sobre a produção de pares de mésons vetoriais $\psi(2S)\phi$ sem atividade adicional nos detectores do experimento LHCb. Os dados utilizados foram obtidos em colisões próton-próton com energia no centro de massa de 13 TeV, registradas durante o Run 2 do LHC (2016–2018), com uma luminosidade integrada de 1,73 fb^{-1}. Os candidatos a $\psi(2S)\phi$ são reconstruídos a partir dos estados finais de decaimento do $\psi(2S)$ e do ϕ, correspondentes a pares de múons e kaons, respectivamente, detectados na região de pseudorapidez $2 < \eta < 5$ e com $p_T > 200$ MeV. O número de candidatos selecionados é 40. A seção de choque fiducial da produção $\psi(2S)(\rightarrow \mu^+\mu^-)\phi(\rightarrow K^+K^-)$ é

$$\sigma_{\psi(2S)\phi} = 0.0723 \pm 0.0117 \text{ pb} \tag{1}$$

onde a incerteza é estatística. Além disso, esta dissertação apresenta uma contribuição para a atualização da implementação do gerador StarLight na simulação do experimento LHCb.

Palavras-chave: Produção central exclusiva, Seção de choque, Mésons vetoriais, Cromodinâmica quântica, Difração, Pomeron, LHCb, Física de altas energias.

Abstract

Associated production of $\Psi(2S)$ and Φ in diffractive proton-proton collisions at the LHCb experiment

Jeferson dos Santos Oliveira

Advisor: Murilo Santana Rangel

Coadvisor: Bruno Souza de Paula

Abstract da Dissertação de mestrado apresentada ao Programa de Pós-Graduação em Física do Instituto de Física da Universidade Federal do Rio de Janeiro - UFRJ, como parte dos requisitos necessários à obtenção do título de Mestre em Ciências (Física).

This dissertation presents the first study on the production of vector meson pairs $\psi(2S)\phi$ without additional activity in the detectors of the LHCb experiment. The data used were obtained from proton-proton collisions with a center-of-mass energy of 13 TeV, recorded during LHC Run 2 (2016–2018), with an integrated luminosity of 1.73 fb^{-1}. The $\psi(2S)\phi$ candidates are reconstructed from the final decay states of the $\psi(2S)$ and ϕ, corresponding to muon and kaon pairs, respectively, detected in the pseudorapidity region $2 < \eta < 5$ and with $p_T > 200$ MeV. The number of selected candidates is 40. The fiducial cross section for the production $\psi(2S)(\rightarrow \mu^+\mu^-)\phi(\rightarrow K^+K^-)$ is

$$\sigma_{\psi(2S)\phi} = 0.0723 \pm 0.0117 \text{ pb} \tag{2}$$

where the uncertainty is statistical. In addition, this dissertation presents a contribution to the update of the STARlight generator implementation within the LHCb experiment simulation framework.

Keywords: Central exclusive production, Cross-section, Vectorial mesons, Quantum Chromodynamics, Diffraction, Pomeron, LHCb, High energy physics.

Acknowledgements

Nos primeiros 1,5 meses, o presente trabalho foi realizado com o apoio da Coordenação de Aperfeiçoamento de Pessoal de Nível Superior (CAPES) e, nos últimos cinco meses, com o apoio do Conselho Nacional de Desenvolvimento Científico e Tecnológico (CNPq).

Agradeço ao meu orientador, professor Murilo Santana Rangel, que, além de orientador, tornou-se um grande amigo - uma pessoa excepcional, que proporcionou momentos únicos, inclusive em experiências internacionais, além de ser um profissional de excelência. Agradeço também ao professor Bruno Souza de Paula, que gentilmente aceitou ser meu coorientador.

Aos secretários da Pós-Graduação da UFRJ, Igor de Souza e Luiza Botelho, que sempre disponibilizaram seu tempo para esclarecer dúvidas e resolver, de forma eficaz, os problemas enfrentados pelos estudantes de pós-graduação, tornando a trajetória pelo mestrado e doutorado muito mais tranquila e agradável.

Aos meus amigos, que tornaram os dias no Fundão ainda mais prazerosos: Gabriella Machado Darze; Dennis Justino de Souza, que esteve comigo durante os dois meses presenciais que passamos no CERN; Jéssica Martins Mafra do Vale; Sarah Sippert; e Alexandre Cardoso Campos.

Aos colegas que me ajudaram nas disciplinas, o que, consequentemente, me permitiu ter tempo para escrever esta dissertação: Leonardo Monteiro Pazito, Welberth Kennedy, Wesley Nascimento, Victor Velasco e Cássia da Silva Nascimento.

Ao Lucas Meyer Garcia, que, além de auxiliar na orientação desta dissertação, me deu dicas e apoio durante minha primeira estadia no CERN.

To Gloria Corti, for making time to teach during my master's studies and for providing me with a truly rewarding experience.

Ao Juan Leite, que me ajudou na implementação do StarLight no framework do Gauss durante o período em que estive no CERN.

A todos os professores do Instituto de Física, pelos ensinamentos e experiências que levarei para toda a vida.

Por fim, a todos aqueles que me ajudaram a trilhar o caminho até aqui, deixo o meu sincero agradecimento.

Contents

List of Figures

List of Tables

Chapter 1

Introduction

The understanding of atomic structure has evolved significantly over time. The earliest concepts date back to ancient Greece, when Democritus proposed that matter is composed of indivisible entities known as atoms. In 1808, John Dalton developed the atomic theory, suggesting that atoms are indivisible, solid spheres that combine in fixed ratios to form matter.

In 1897, J.J. Thomson, through his cathode ray experiments, discovered the electron, revealing that atoms are divisible and contain negatively charged particles. This led to the "plum pudding" model, in which the atom is envisioned as a positively charged sphere with embedded negatively charged electrons.

In 1909, Ernest Rutherford conducted the gold foil experiment, demonstrating that atoms possess a small, dense, positively charged nucleus. This gave rise to the nuclear model of the atom, where electrons orbit the nucleus similarly to planets orbiting the Sun.

However, Rutherford's model could not explain atomic stability or discrete spectral lines. In 1913, Niels Bohr introduced the concept of quantized electron orbits, giving rise to the Bohr model, which successfully explained the spectral lines of hydrogen. Nevertheless, this model failed for atoms with more than one electron.

In the 1920s, the development of quantum mechanics, with Erwin Schrödinger's wave mechanics and Werner Heisenberg's matrix mechanics, replaced the concept of defined electron orbits with probabilistic distributions known as orbitals. This framework successfully explained atomic spectra and electron behavior, incorporating principles such as the Pauli exclusion principle and electron spin.

In 1932, James Chadwick discovered the neutron, leading to the understanding that atomic nuclei are composed of protons and neutrons, bound by the strong nuclear force. In the mid-20th century, the comprehension of interactions at atomic scales advanced with the development of Quantum Electrodynamics (QED). As numerous new particles were discovered, the Standard Model of Particle Physics was formulated, describing matter in terms of quarks, leptons, and gauge bosons. The discovery of the Higgs boson in 2012 confirmed the mechanism responsible for mass generation.

Although the Standard Model successfully describes known particles and fundamental forces - except gravity - many questions remain unanswered, such as the nature of dark matter, the origin of neutrino masses, and the search for physics beyond the Standard Model. Experiments like those conducted at the LHC are essential to deepen our understanding of matter and to search for new particles and interactions.

In the 1960s, Murray Gell-Mann and George Zweig proposed the quark model. They suggested that hadrons are composed of quarks, where mesons are formed by a quark-antiquark pair ($q\bar{q}$), and baryons are composed of three quarks (qqq). The $\psi(2S)$ meson is an excited state of the J/ψ meson, known as a charmonium state, formed by a charm quark and a charm antiquark ($c\bar{c}$). On the other hand, the ϕ meson is composed of a strange quark and a strange antiquark ($s\bar{s}$).

This dissertation focuses on the study of the associated production of these mesons, $\psi(2S)\phi$, in a diffractive process known as Central Exclusive Production (CEP). In CEP, the two incoming protons either remain intact or dissociate into very low-mass systems, while the central system (in this case, the meson pair) is produced through a colorless exchange, typically described by pomeron exchange. A key characteristic of CEP events is the presence of large rapidity gaps between the centrally produced system and the outgoing protons; these regions are devoid of hadronic activity and correspond to areas with no detector signals. This clean experimental environment is ideal for studying meson production mechanisms, testing Quantum Chromodynamics (QCD) in the non-perturbative regime, and gaining further insights into the nature of pomeron exchange.

In this work, $\psi(2S)\phi$ candidate events with no additional activity in the LHCb detector are investigated. In addition, contributions to the STARlight [1] simulation are presented.

Chapter 2

Theoretical Oveview

This chapter provides an overview of the theoretical concepts underlying the $\psi(2S)\phi$ data analysis presented in this dissertation. The Standard Model of particle physics (SM) will be briefly introduced, highlighting its fundamental particles and interactions, with special emphasis on the description of strong interactions and the challenges posed by Quantum Chromodynamics in the non-perturbative regime. The discussion is not intended to be exhaustive; rather, it focuses on the key aspects most relevant to this analysis. For comprehensive treatments of the Standard Model, the reader is referred to [2], while for diffraction physics and Regge theory, the specialized literature in [3] provides further details.

The associated production of $\psi(2S)\phi$ in diffractive processes, specifically Central Exclusive Production (CEP), will then be discussed, detailing the characteristic features of CEP events, such as the presence of large rapidity gaps and the colorless exchange mechanisms responsible for the exclusive production of the central system. In addition, the theoretical framework of high-energy diffraction will be introduced, including the basics of Regge theory, which provides an effective description of diffraction processes through the exchange of trajectories like the pomeron.

Quantum Chromodynamics (QCD)

Quantum Chromodynamics is a theoretical model for the strong force, explaining the interactions between quarks and gluons. In QCD, there are eight massless particles known as gluons, and six spin-1/2 fermions called quarks. QCD involves changes in color charge, similar to the change of electric charge in Quantum Electrodynamics. However, unlike QED, in QCD not only the fermions transfer charge - both quarks and gluons change color charge. This difference arises because gluons carry color charge, unlike the photon.

The mediators of the strong force are the gluons. There are a total of $N_C = 3$ color charges: blue, green, and red. There are three families, each containing two types of quarks: up-type and down-type. Up-type quarks have a charge of $+2/3$, and down-type quarks have a charge of -1/3. The positively charged quarks are up (u), charm (c), and top (t), while the negatively charged quarks are down (d), strange (s), and bottom or beauty (b).

The antiquark has the same mass and spin properties as the quark, but with opposite quantum numbers. For example, a quark up has electric charge +2/3, while an antiquark up has electric charge -2/3; a strange quark has strangeness -1, and an anti-strange quark has strangeness $+1$ (see Table 2.1 for the quark quantum numbers). If a quark has the color charge blue, the corresponding antiquark has the anti-blue color charge. A quark-antiquark pair can form a meson, such as the $\psi(2S)$, which consists of a charm quark and an anti-charm quark ($c\bar{c}$).

Quark	**u**	**d**	**c**	**s**	**t**	**b**
Electric charge (e)	$+\frac{2}{3}$	$-\frac{1}{3}$	$+\frac{2}{3}$	$-\frac{1}{3}$	$+\frac{2}{3}$	$-\frac{1}{3}$
Isospin (I)	$\frac{1}{2}$	$\frac{1}{2}$	0	0	0	0
I_3	$+\frac{1}{2}$	$-\frac{1}{2}$	0	0	0	0
Strangeness (S)	0	0	0	-1	0	0
Charm (C)	0	0	$+1$	0	0	0
Bottomness (B')	0	0	0	0	0	-1
Topness (T)	0	0	0	0	$+1$	0

Table 2.1: Quarks up (u), down (d), charm (c), strange (s), top (t) and bottom or beauty (b) and their quantum numbers: electric charge, isospin, I z-component, strangeness, charm, bottomness, and topness.

QCD is a non-Abelian gauge theory based on the special unitary symmetry group of degree three, $SU(3)_C$. $SU(3)$ refers to the group of complex $3{\times}3$ unitary matrices with determinant 1. This group has eight generators, corresponding to the eight gauge bosons - the gluons - of the strong interaction. The subscript “C” indicates that QCD applies only to particles that carry color charge.

Gluons carry both color and anti-color charges, enabling them to interact not only with quarks but also with other gluons. This self-interaction property is a distinctive feature of QCD and leads to the phenomenon of color confinement. As a result, the strong interaction becomes stronger with increasing separation between quarks, preventing their isolation and ensuring they remain bound within color-neutral hadrons.

In QCD, every elementary particle is associated with a field that extends throughout all space-time. If distinct configurations of these fields result in identical measurements of observables, the field is said to be gauge invariant under that gauge transformation. The Lagrangian density, $\mathcal{L}$, governs the dynamics of the theory, i.e., how the fields evolve over time and interact with each other.

2.1 QCD Lagragian

The triplet form is used to interpret the quark (anti-quark) field $\psi_i(\bar{\psi}_i)$.

$$\psi_i = \begin{bmatrix} \psi_1 \\ \psi_2 \\ \psi_3 \end{bmatrix} \text{ and } \bar{\psi}_i^* = \begin{bmatrix} \bar{\psi}_1^* \\ \bar{\psi}_2^* \\ \bar{\psi}_3^* \end{bmatrix}, \tag{2.1}$$

and the numbers represent the three color charges. The gauge transformation of the fermion wave function is given by

$$\psi(x) \to \psi'(x) = e^{ig_s\theta^a(x)\cdot T^a}\psi(x) \tag{2.2}$$

where g_s is the strong coupling constant, and the index a in $\theta^a(x)$, with $a = \{1, \dots, N_C^2 - 1 = 8\}$, corresponds to the eight possible gluons. The $\theta^a(x)$ are eight phase factors that depend on space-time coordinates, and T_a denotes the generator of the gauge group, referred to as the colour-charge matrix. The matrix T_a is related to the Gell-Mann matrices λ_a (see equations 2.3–2.5), and is a Hermitian 3×3

matrix (see equation 2.6). The Gell-Mann matrices are a set of eight 3×3 Hermitian, traceless matrices that serve as the generators of the Lie algebra of $SU(3)$, the gauge group of QCD. They are the analogues of the Pauli matrices (which generate $SU(2)$), but for $SU(3)$.

$$\lambda^1 = \begin{pmatrix} 0 & 1 & 0 \\ 1 & 0 & 0 \\ 0 & 0 & 0 \end{pmatrix}, \quad \lambda^2 = \begin{pmatrix} 0 & -i & 0 \\ i & 0 & 0 \\ 0 & 0 & 0 \end{pmatrix}, \quad \lambda^3 = \begin{pmatrix} 1 & 0 & 0 \\ 0 & -1 & 0 \\ 0 & 0 & 0 \end{pmatrix} \tag{2.3}$$

$$\lambda^4 = \begin{pmatrix} 0 & 0 & 1 \\ 0 & 0 & 0 \\ 1 & 0 & 0 \end{pmatrix}, \quad \lambda^5 = \begin{pmatrix} 0 & 0 & -i \\ 0 & 0 & 0 \\ i & 0 & 0 \end{pmatrix}, \quad \lambda^6 = \begin{pmatrix} 0 & 0 & 0 \\ 0 & 0 & 1 \\ 0 & 1 & 0 \end{pmatrix} \tag{2.4}$$

$$\lambda^7 = \begin{pmatrix} 0 & 0 & 0 \\ 0 & 0 & -i \\ 0 & i & 0 \end{pmatrix}, \quad \lambda^8 = \frac{1}{\sqrt{3}} \begin{pmatrix} 1 & 0 & 0 \\ 0 & 1 & 0 \\ 0 & 0 & -2 \end{pmatrix} \tag{2.5}$$

$$T^a = \frac{1}{2}\lambda^a. \tag{2.6}$$

Taking into account that the group generators do not commute, so the commutation results

$$[T^a, T^b] = if^{abc}T^c, \tag{2.7}$$

and that means the group is non-Abelian. The colour structure constants, f^{abc}, with indices a, b, and c, which can take the value of any eight colour degrees of freedom, are a factor of the commutator.

The gamma matrices are denoted by γ_μ[1], and the four-gradient is given by $\partial^\mu = (\partial_t, -\vec{\nabla})$. To ensure local gauge invariance under $\mathrm{SU}(3)_C$, it becomes necessary to introduce a new gauge field, known as the gluon field, which has one time-like and three space-like components. These components are organized into an octet structure, A^μ_a, where $a = 1, \ldots, 8$ corresponds to the eight generators of the SU(3) group. To preserve gauge invariance, the ordinary derivative ∂^μ must be replaced by the covariant derivative D^μ, which incorporates the gluon fields and maintains the symmetry of the theory

$$\partial_\mu \to D_\mu = \partial_\mu + ig_s A^a_\mu T^a, \tag{2.8}$$

[1]They appear in the Dirac equation, which describes relativistic spin-1/2 particles such as electrons and quarks.

where covariant derivative, denoted by D_μ, modifies the ordinary derivative by including the gluon fields, enabling the interaction between quarks and gluons. This leads to the quark-quark-gluon interaction vertex, which represents a fundamental point in Feynman diagrams where two quark lines and one gluon line meet, describing the exchange of color charge. Additionally, the gluon field strength tensor $F_a^{\mu\nu}$ characterizes the dynamics of the gluon fields and their self-interactions. It is defined by combining derivatives of the gluon fields and nonlinear terms involving the gluon fields themselves, reflecting the non-Abelian nature of QCD and ensuring the proper description of how gluons interact with each other and with quarks.

$$F_a^{\mu\nu} = \partial^\mu A_a^\nu - \partial^\mu A_a^\mu + g_s f^{abc} A_b^\mu A_c^\nu. \tag{2.9}$$

Since gluons carry color charge and the generators of the SU(3) gauge group do not commute, the gluon fields interact with each other. This self-interaction is represented by the third term in the gluon field strength tensor, $g_s f^{abc} A_b^\mu A_c^\nu$. Unlike photons in electromagnetism, which do not interact with themselves because the U(1) group is Abelian (commutative), gluons in QCD exhibit nonlinear interactions. These self-interactions give rise to additional vertices in Feynman diagrams: one vertex involving three gluons and another involving four gluons. These multi-gluon vertices are crucial for understanding the complex behavior of the strong force, including phenomena such as gluon confinement and asymptotic freedom.

The QCD Lagrangian density gives the dynamics of quarks and gluons and is writen as

$$\mathcal{L}_{QCD} = \sum_f \bar{\psi}_f^i (i\gamma_\mu D^\mu - m_f)_{ij} \psi_f^j - \frac{1}{4} F_a^{\mu\nu} F_{\mu\nu}^a, \tag{2.10}$$

and the symbol of fermion masses is m_f. The gluons are massless, and it can be seen by looking at the Lagrangian and realizing that there is no term of the format $m^2 A^\mu A_\mu$.

2.2 Color confinement

A gluon carrying two different color charges mediates the strong interaction between two quarks. When the protons collide in LHCb, numerous jets of quarks are produced, which subsequently hadronize - that is, the quarks form bound states known as hadrons. A quark and an antiquark can hadronize into a meson; for example, a charm quark c can combine with an anti-charm quark $\bar{c}$ to form a $\psi(2S)$ meson.

As the distance between two quarks within a hadron increases, additional gluons can interact among themselves via virtual gluons mediating the strong force, causing the energy of the system to grow. When this energy becomes large enough, it can create a new quark-antiquark pair. This explains why quarks cannot be observed in isolation - a phenomenon known as color confinement. At a higher energy a quark-antiquark pair can split multiple times, generating jets of different particles.

Hadrons are classified as mesons, consisting of quark-antiquark pairs ($q\bar{q}$), and baryons, composed of three quarks (qqq) or three antiquarks ($\bar{q}\bar{q}\bar{q}$), all of which are color-neutral. Recently, exotic hadrons have been discovered, which can be interpreted as tetraquark states ($qq\bar{q}\bar{q}$) or pentaquark states ($qqqq\bar{q}$) (see Refs. [4, 5]).

2.3 Asymptotic freedom

The strong coupling constant, α_s, expresses the strength of the strong interaction between quarks and gluons. This constant has an effective value obtained experimentally and varies with the energy scale - it becomes smaller at higher energies due to asymptotic freedom. This effective value is different from the one used in Feynman diagrams, which often adopt a standard value or a perturbative expansion to simplify the calculations.

The fields of fermions and bosons are subject to quantum fluctuations, meaning that virtual quarks and gluons can momentarily emerge around a quark. These virtual particles can interact with the probe quark, influencing its properties through short-lived quantum effects. In this cloud of electric and color charge, quark-antiquark pairs can be created, and the antiquark is closer to the probe quark.

This phenomenon is known as vacuum polarization. In quantum field theory, the vacuum is not empty but filled with quantum fluctuations, allowing virtual particles - such as quark-antiquark pairs and gluons - to temporarily emerge and interact. These fluctuations modify the strength of the strong interaction, represented by the coupling constant g_s. At large distances (or low energies), virtual gluon interactions enhance the effective value of g_s, making the strong force more intense, whereas at short distances (or high energies), gluon self-interactions reduce the effective coupling, leading to asymptotic freedom, a key feature of QCD where quarks behave almost as free particles when they are extremely close to each other. Empirically, the four-momentum transfer $Q^2 = -q^2$ increases as we probe smaller distances in particle interactions, establishing a direct correlation between g_s and the energy scale: as Q^2 increases, the effective value of g_s decreases (asymptotic freedom), while at lower Q^2 it increases, resulting in color confinement, the phenomenon that prevents quarks from existing in isolation.

In a Feynman diagram, such as the scattering of two quarks mediated by a gluon (see Figure 2.1), quantum corrections arise due to virtual particles and loop processes. These corrections often lead to divergences in the calculations. To fix this, a procedure called renormalization is applied, which systematically removes these infinities by redefining the physical parameters of the theory, such as masses and coupling constants. As a result, the strong coupling constant becomes scale-dependent, leading to what is known as the running coupling constant. This means that the effective strength of the strong interaction varies with the energy scale of the process, decreasing at high energies (or short distances), a phenomenon known

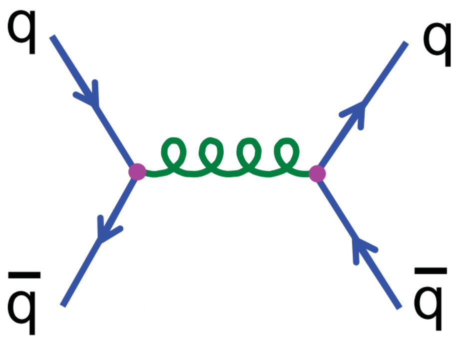

Figure 2.1: Scattering of two quarks mediated by a gluon. Extracted from [6].

as asymptotic freedom.

$$\alpha_S(Q^2) = \left[\frac{11N_C - 2N_f}{12\pi} \ln\left(\frac{Q^2}{\Lambda^2}\right)\right]^{-1}, \tag{2.11}$$

with N_C representing the number of colour charges, which is 3, N_f is the quark number, which is equal to 6, Q is the four-momentum transfer due to the interchange of gluons, and Λ is the QCD energy scale parameter, and with that value it is possible to know when $\alpha_s(Q^2)$ diverge asymptotically.

2.4 Pomeron

The pomeron is a theoretical construct used to describe high-energy hadronic interactions where no quantum numbers are exchanged between the incoming and outgoing particles. It is interpreted as a colour-singlet state composed of two gluons [7], carrying the same quantum numbers as the vacuum. Specifically, the pomeron is characterized by having no electric charge, an isospin of $I = 0$, parity $P = +1$, and charge conjugation $C = +1$. The absence of electric charge implies that it does not couple directly to photons. The isospin value $I = 0$ indicates that it is an isoscalar state, exhibiting no preference between up and down quark components. The positive parity ($P = +1$) means that its wave function remains unchanged under spatial inversion, while the positive charge conjugation ($C = +1$) shows that the pomeron is symmetric under the exchange of particles and antiparticles. As a result, processes mediated by pomeron exchange do not alter the internal quantum numbers of the interacting hadrons.

The origin of the pomeron lies in Regge theory, which extends the concept of angular momentum in quantum mechanics to complex values. This theoretical framework was initially developed to model scattering amplitudes and was later successfully adapted to the relativistic regime, where it was applied to hadron-hadron and photon-hadron collisions at high energies.

In Regge theory, the scattering amplitude is described in terms of Regge trajectories, which are analytic functions relating the angular momentum J of a family of particles to their squared masses m^2. Each trajectory corresponds to a family of hadronic resonances with similar properties. However, experimental data on total cross-sections at high energies showed that they do not decrease with energy as expected from known trajectories. To resolve this discrepancy, a new Regge trajectory was introduced - the pomeron trajectory. Unlike other trajectories, the pomeron does not correspond to any known family of particles, but its inclusion is essential to describe the observed slowly rising or constant behavior of total cross-sections in high-energy hadronic scattering.

From a QCD perspective, the pomeron is often modeled as the exchange of two or more gluons in a colorless configuration, making it compatible with the observed color neutrality and the preservation of quantum numbers in the final state. This interpretation connects Regge theory with both perturbative and non-perturbative aspects of QCD, particularly in the context of diffractive processes and central exclusive production.

2.5 Central exclusive production

When the protons scatter at small angles and keep intact, producing a system with one or two particles, this is characterized as CEP. Where the system X is located in the central region, at near-zero rapidity with respect to the initial protons, and contains only the exclusive products of its own decays, with no other hadronic interactions. Rapidity is a quantity that gives the information about the coverage of the detector and is useful because it is invariant under longitudinal relativistic transformation and can be written as

$$y = \frac{1}{2} \ln \left(\frac{E + p_z c}{E - p_z c} \right), \tag{2.12}$$

where E is the energy of the produced particle, p_z is the momentum projected on the beamline, and c is the speed of light in vacuum. If there is no momentum projected on the beamline, the rapidity is zero, and it increases according to the growth of the p_z, as can be seen in eq 2.12. If the momentum is greater than the mass of the particle, the rapidity approaches the pseudorapidity

$$\eta = -\ln \tan \left(\frac{\theta}{2} \right) \tag{2.13}$$

where θ is the polar angle evaluated starting from the z-axis.

In LHCb, CEP events have two rapidity gaps, which are spaces of inactivity in the detector and are symbolized by $\oplus$, at the volume around the system of interesting and outgoing protons

$$p_1 \oplus p_2 \to p_3 \oplus X \oplus p_4, \tag{2.14}$$

where p_1 and p_2 are the colliding protons and p_3 and p_4 are the scattering protons. Therefore, there are two rapidity-gap criteria in CEP without pile-up or secondary interactions. Thus, CEP affords a quietly empty habitat to analyze the signal with special kinematic and dynamic constraints that are independent of the central system, in a good approximation. Furthermore, it is possible to obtain physics information like spin and parity quantum numbers that is hard to acquire through inelastic events.

Studying CEP makes it possible to know quantum properties of the system, know more about resonant and non-resonant states, and glueball[2] and odderon[3] of the Standard Model (SM). It is also possible to work in states beyond the standard model.

[2]A glueball is a hypothetical bound state composed entirely of gluons, without valence quarks.

[3]The odderon is a theoretical Regge trajectory in QCD corresponding to the exchange of a colorless state with negative charge conjugation parity (C=-1), typically modeled as three gluons in a symmetric color-singlet configuration.

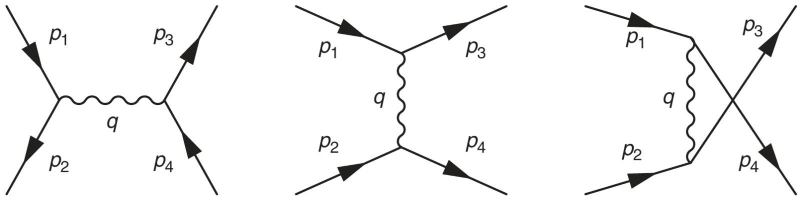

Figure 2.2: The Feynman diagrams for the s-channel, t-channel, and u-channel processes. The u-channel diagram applies only when identical particles appear in the final state. Extracted from [8].

2.6 CEP production mechanisms

In particle physics, the s-channel, t-channel, and u-channel are ways to classify interaction processes based on the Mandelstam variables (see Fig.2.2). The s-channel describes a process where two particles collide and form an intermediate resonance that then decays into final products. It depends on the total energy squared s. The t-channel involves the exchange of a virtual particle between an initial and a final particle, related to momentum transfer t. It is common in scattering processes. The u-channel is similar to the t-channel but involves a different particle exchange configuration, associated with the variable u, often relevant when identical particles are involved.

CEP occurs in the t-channel, where each proton can emit another particle that is absorbed by the other proton, and that way the proton remains intact, which is not viable in the s-channel and u-channel. Since there is no exchange of electric or color charge in the t-channel, just color singlets (particles or systems with a total color charge of zero) are emitted. As a result, the protons keep intact and conserve the rapidity gap of the final state.

Double-photon exchange

CEP can occur with double-photon exchange, and this mechanism is explained by quantum electrodynamics. In this process, both protons emit a quasi-real photon (low-Q^2), where q is the transference of four-momentum from the proton to the photon. In this mechanism, it is viable to study non-resonant states like light-by-light ($\gamma\gamma \to \gamma\gamma$) scattering, di-electron ($\gamma\gamma \to e^+e^-$), and di-muon ($\gamma\gamma \to \mu^+\mu^-$). Also, it is useful to investigate the boson pair production ($\gamma\gamma \to W^+W^-$), meson production like $\gamma\gamma \to \eta_c$, and double-hadron ($\gamma\gamma \to hh$).

Photo-production

Another mechanism of CEP is a production in which one proton emits a pomeron and the other emits a photon. The odd-charge-conjugate of the photon with the even-charge-conjugate of the pomeron makes it possible to investigate odd-charge-conjugate entities, allowing the study of spin-1 vector meson final states (1^{-}) like $\gamma\mathcal{P} \to \rho^0$. This aids the field of heavy-quarkonia states, $c\bar{c}$ and $b\bar{b}$, such as $\gamma\mathcal{P} \to J/\psi$, $\psi(2S)$, and $\gamma\mathcal{P} \to \Upsilon(1S)$ mesons.

These states are in the field of pQCD[4] and are of use to examine small Bjorken-x, that is, how much momentum from the proton the parton (quarks and gluons) keeps for itself. Since the odderon-pomeron ($O\mathcal{P} \to X$) can contribute to the cross-section of vector meson CEP, quarkonium studies become valuable tools for investigating the existence of the odderon, a hypothetical state with odd charge conjugation ($C = -1$). Additionally, this framework allows for the exploration of heavier states, such as the neutral Z^0 boson.

Double-pomeron exchange

CEP also can occur in double-pomeron interaction, where both of the protons emit a pomeron. Since both pomerons are even-charge-conjugate, it is viable to access even-charge-conjugate particles. There are some constraints in this CEP process that permit just a specific number of particles, as those with $J^{CP} = 0^{++}$, 1^{++}, 2^{++}, ... and isospin $I = 0$. Furthermore, it is possible to study χ_c and χ_b mesons.

CEP is useful to find out new particles, such as glueball candidates like $f_0(1500)(0^{++})$

[4]In energy regimes where the strong coupling α_s is small, theoretical calculations can be performed using perturbative series expansions [9].

and $f_0(1710)(0^{++})$. Because, as predicted by lattice QCD, the lightest glueball state must be low-mass $\approx$ 1700 MeV and quantum number 0^{++} [10, 11, 12], which makes $f_0(1500)(0^{++})$ and $f_0(1710)(0^{++})$ good candidates.

The double pomeron exchange can decay in di-jet ($\mathcal{PP} \rightarrow jj$), thus it can produce Higgs boson $\mathcal{PP} \rightarrow H^0 \rightarrow b[j]\bar{b}[j]$, and regarding it is possible to know the value of the spin in the central system, it is a great manner to test our Higgs boson results.

2.7 CEP kinematics and dynamics

2.7.1 Bjorken-x in deep inelastic scattering

In deep inelastic scattering, a high-energy charged particle collides with a nucleon, probing its internal structure through the exchange of a virtual gauge boson with four-momentum q. This process is characterized by a variable called Bjorken-x [3]

$$x \equiv \frac{Q^2}{2P \cdot q}. \tag{2.15}$$

the variable Q refers to the four-momentum of the gauge boson, in a manner that

$$Q^2 = -q^2, \tag{2.16}$$

and P is the high-energy charged hadron that strikes the nucleon. The relation between the wavelength of the virtual gauge boson and its four-momentum is given by:

$$\lambda = \frac{h}{p}, \tag{2.17}$$

where h is Planck's constant. When Q^2 is low, it is possible to probe the overall size of the proton. At higher Q^2, the associated wavelength becomes smaller, allowing the internal structure of the proton to be resolved.

There is an independence between the structure functions' dependence on Bjorken-x and the resolution scale of the exchanged boson (i.e., the momentum transfer of the probe particle), known as Bjorken scaling. This behavior suggests that the hadrons are composed of point-like constituents called partons, such as quarks and gluons.

Bjorken-x in double-pomeron exchange

The double pomeron exchange mechanism in CEP serves as a valuable probe of different regimes of QCD. At high values of the momentum transfer squared (Q^2), corresponding to a large invariant mass of the central system (m_X) - such that $Q^2 \gg \Lambda^2_{QCD}$, where Λ_{QCD} is the QCD energy scale - and the strong coupling constant α_s becomes small. This places the process within the domain of pQCD, where theoretical predictions can be safely obtained using series expansions. However, at low Q^2, the interaction enters the non-perturbative regime, where pQCD is no longer valid. In this domain, additional soft interactions - known as reinteraction or rescattering corrections - may occur, filling the rapidity gaps with hadronic activity and thus violating the defining signature of CEP. To describe such phenomena, Regge theory becomes an appropriate framework, offering insight into low-energy QCD processes. In particular, the behavior of parton distribution functions (PDFs), especially those of gluons at small values of Bjorken-x and Q^2, becomes crucial. These PDFs describe the probability of finding a parton carrying a fraction x of the proton's energy and are determined from global fits to experimental data, carry large uncertainties in this phase-space region, impacting both Standard Model predictions and searches for new physics. Consequently, double pomeron exchange provides a unique opportunity to test QCD dynamics across a wide range of energy scales.

The square of the center-of-mass energy, s, is calculated by:

$$s = (p_1 + p_2)^2, \tag{2.18}$$

where p_1 and p_2 represent the momentum of the incoming protons. If the proton masses are ignored, then the quark masses are also neglected, and the four-momenta of the partons in the hadron center-of-mass frame are:

$$p_a = \frac{\sqrt{s}}{2}(x_a, 0, 0, x_a) \text{ and } p_b = \frac{\sqrt{s}}{2}(x_b, 0, 0, -x_b), \tag{2.19}$$

In the double pomeron exchange approximation, x_a and x_b can be described as fractions of the energies of the incoming protons, p_1 and p_2. In this way, the mass of the central system, m_X, can be expressed as:

$$m_X^2 = (p_a + p_b)^2 = x_a x_b s. \tag{2.20}$$

Considering this approach, the rapidity of the central system can be written as:

$$y = \frac{1}{2}\ln\left(\frac{E + p_z}{E - p_z}\right) = \frac{1}{2}\ln\left(\frac{E\ (x_a + x_b + x_a - x_b)}{E\ (x_a + x_b - x_a + x_b)}\right) = \frac{1}{2}\ln\left(\frac{x_a}{x_b}\right), \tag{2.21}$$

in which E is the energy of the central system and p_z is its longitudinal momentum. The partons' momenta can be written in terms of the center-of-mass energy, as well as the mass and rapidity of the central system

$$x_a = \frac{m_X}{\sqrt{s}}e^{+y} \quad \text{and} \quad x_b = \frac{m_X}{\sqrt{s}}e^{-y}. \tag{2.22}$$

The topology of LHCb, covering the rapidity range of $2.0 < y < 4.5$, is useful for studying Bjorken-x at both low and high values. The phase space coverage in the x vs. Q^2 plane is shown in the figure 2.3.

2.8 Typically low p_T^2 in CEP

The creation of a meson via the CEP process occurs through the exchange of a colourless object in the t-channel. The differential cross-section of elastic pp scattering, in terms of the momentum difference between the incoming and outgoing protons (t), which is one of the three Mandelstam variables (s, t, and u), decreases as $|t|$ increases [14]. The squared momentum transfer is

$$t = (p_1 - p_3)^2 = (p_4 - p_2)^2, \tag{2.23}$$

such that the four-momenta of the incoming and outgoing protons are p_1, p_2 and p_3, p_4, respectively. In elastic processes, as an initial approximation, the cross-section can be written in terms of the Mandelstam variable t.

$$\frac{d\sigma}{dt} \propto e^{-b_{CEP}|t|}, \tag{2.24}$$

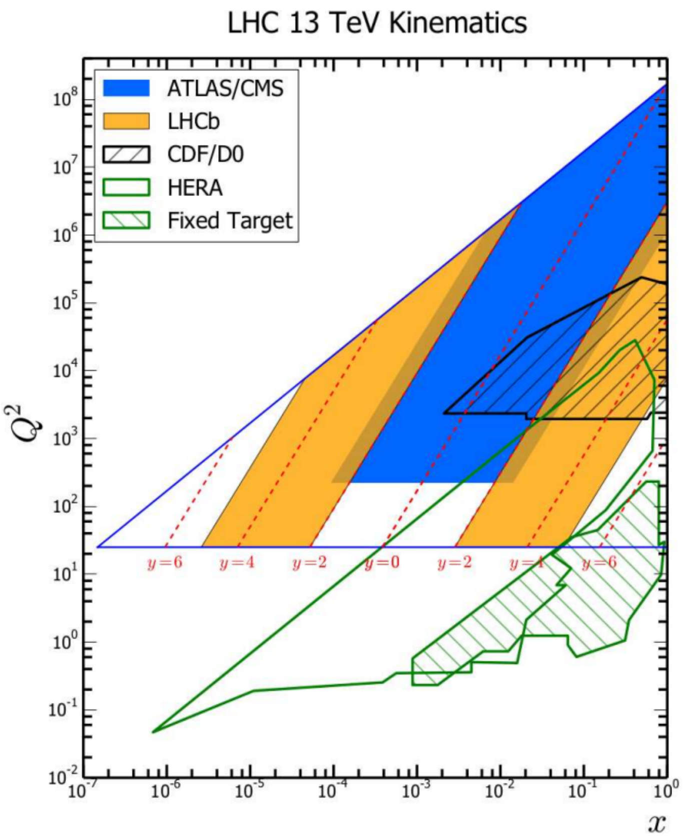

Figure 2.3: Kinematic coverage in the (x, Q^2) phase space for proton-proton collisions at $\sqrt{s} = 13$ TeV, compared to the coverage achieved by ATLAS, CMS, CDF/D0, HERA, and fixed-target experiments. Extracted from [13].

where the validity of this expression is approximately for $|t| < 0.5$ GeV/c, in which b_{CEP} is the exponential slope. In the case of inelastic processes, the cross-section exhibits a similar behavior, but the decay rate is lower

$$\frac{d\sigma}{dt} \propto \left(1 + \left(\frac{b_{In.}}{n}\right)|t|\right)^{-n}, \tag{2.25}$$

for which n is the exponent of the factor. If only low t values are considered, the expression reduces to the previous one

$$\frac{d\sigma}{dt} \propto e^{-b_{In.}|t|}, \tag{2.26}$$

in which $b_{In.}$ is the slope parameter of the exponential in the inelastic process.

Since $|t|$ cannot be calculated empirically, the squared transverse momentum of the central system, X, is computed in the laboratory frame.

$$t \approx -p_T^2(X). \tag{2.27}$$

Inelastic scattering produces particles with high $p_T^2(X)$, causing one or both protons to break up. This is different from the CEP mechanism, which has a constraint on the momentum transfer squared and provides a clean environment to distinguish signal from background.

The study of the CEP production of $J/\psi\phi$ at LHCb has already been conducted, leading to the observation of exotic state production (see [15]). In this work, the study of the $\psi(2S)\phi$ system is presented, where the $\psi(2S)$ decays into a muon pair and the ϕ decays into a kaon pair. The $\psi(2S)$ and ϕ are produced in a CEP process of the photo-production type. The Feynman diagram illustrating an example of double vector meson production is shown in Fig. 2.4.

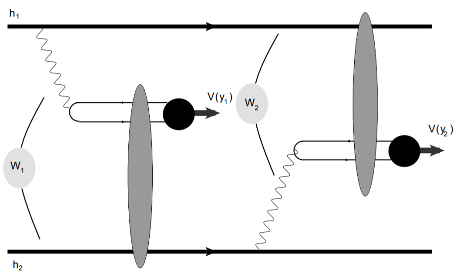

Figure 2.4: Feynman diagram illustrating an example of double vector meson production. Extracted from [16].

Chapter 3

LHCb experiment

The Large Hadron Collider (LHC) is the world's largest particle accelerator. It is located about 100 m underground, within a tunnel previously used by the Large Electron-Positron Collider (LEP). The LHC is located at CERN (the European Organization for Nuclear Research) in Geneva and extends across the border between Switzerland and France [17].

The LHC started its operation with proton-proton (pp) collisions at center-of-mass energies of 7 TeV (2010) and 8 TeV (2012), and 2.76 TeV for lead-lead (PbPb) collisions. This data taking period is known as Run 1. After a two year shutdown to increase the beam energy, Run 2 took place from 2015 to 2018, during which proton collisions reached 13 TeV and PbPb collisions 5.02 TeV. Following a three-year shutdown for further upgrades, Run 3 began in 2022 with a center-of-mass energy of 13.6 TeV for pp collisions and 5.36 TeV for PbPb. There are four interaction points where the four main LHC experiments are built: ATLAS, CMS, LHCb and ALICE.

The four main experiments have different purposes: ATLAS and CMS are general-purpose experiments designed to collect data at high instantaneous luminosity in order to study a wide range of phenomena, including the search for new particles, the Higgs boson, extra dimensions, and potential dark matter candidates. LHCb focuses on heavy-quark physics and operates at lower instantaneous luminosity, with the goal of exploring flavor physics and CP violation. ALICE is dedicated to heavy-ion collisions, investigating the quark-gluon plasma and the state of matter that

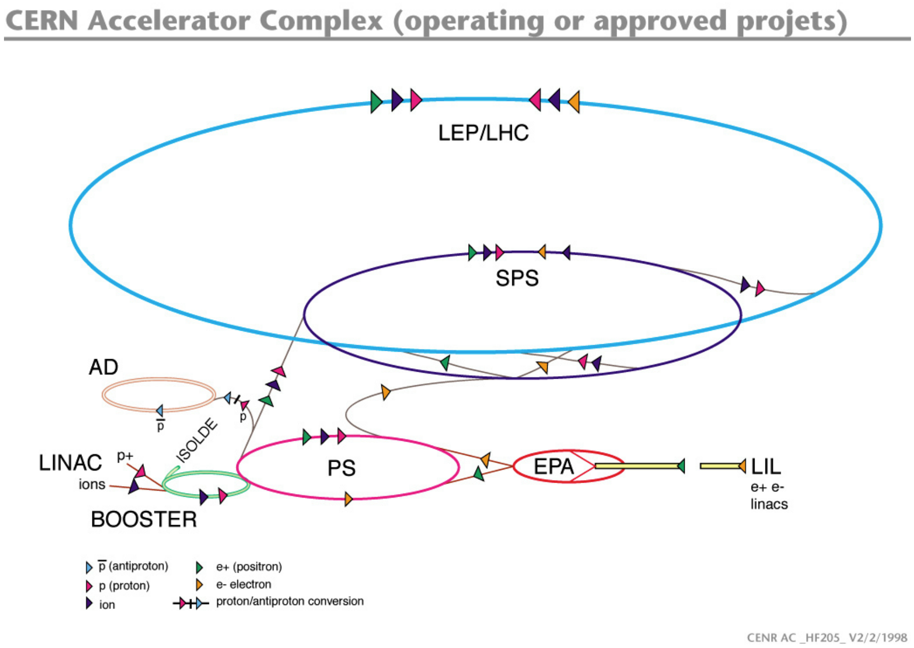

Figure 3.1: CERN accelerator complex. Extracted from [22].

existed shortly after the Big Bang [18].

At the LHC, protons originate from hydrogen gas and pass through several acceleration stages. First, $LINAC_4$ accelerates hydrogen ions (H^-) to 160 MeV. These ions are then sent to the Proton Synchrotron Booster which are accelerated to 2 GeV. Next, the protons enter the Proton Synchrotron (PS) and are accelerated to 26 GeV. They then proceed to the Super Proton Synchrotron (SPS), receiving a further boost to 450 GeV. Finally, the protons are injected into the LHC and accelerated to their maximum energy using radio-frequency cavities (see Figure 3.1). The proton path is precisely guided by superconducting magnets [19, 20].

Collisions occur as follows: two beams of protons travel in opposite directions inside separate beam pipes. Each beam consists of 2,808 bunches, each containing approximately 10^{11} protons. The bunches are spaced 25 nanoseconds apart, resulting in a bunch-crossing frequency of about 40 MHz and a bunch crossing rate of approximately 30 MHz [21].

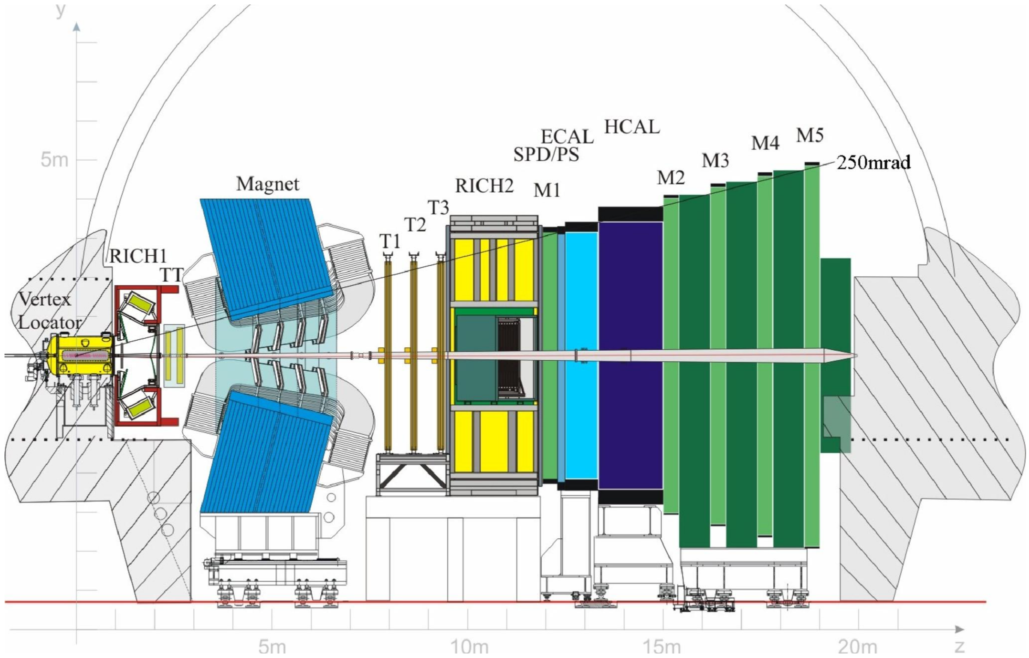

Figure 3.2: LHCb Run 2. Extracted from [24]. The z-axis is aligned along the beam pipe, the perpendicular x-axis points toward the center of the LHC, and the y-axis, perpendicular to both x- and z-axes, points upward.

3.1 LHCb Experiment

LHCb focuses on CP violation and the study of rare decays of b and c hadrons. It is a single-arm forward spectrometer operating within a pseudorapidity range of $2 < \eta < 5$.

The components along the beam line include: the Vertex Locator (VELO), the first Ring Imaging Cherenkov detector (RICH1), the Trigger Tracker (TT), the magnet, three tracking stations (T1, T2, T3), the second Ring Imaging Cherenkov detector (RICH2), the first muon station (M1), the electromagnetic calorimeter (ECAL), the hadronic calorimeter (HCAL), and four additional muon stations (M2, M3, M4, M5). These elements can be classified into four subsystems: the magnet, the tracking system, the particle identification system, and the trigger system [23]. Figure 3.2 shows a schematic description of the LHCb experiment.

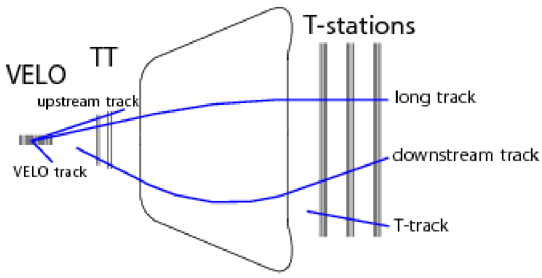

Figure 3.3: Tracking system. Extracted from [31].

3.1.1 Tracking System

A magnetic field of 4 T·m, generated by a dipole magnet [25], bends the trajectories of particles in order to determine their mass, momentum, and to reconstruct the positions of pp collisions and decay vertices. To achieve this, it is necessary to combine information from the Vertex Locator (VELO) [26], the Trigger Tracker (TT) [27], and the inner [28] and outer trackers [29, 30] (see Figure 3.3). The VELO consists of silicon tracking stations surrounding the pp interaction region. The TT provides tracking information upstream of the magnet, while the inner and outer tracking stations are located downstream of the magnet.

3.1.2 Magnet

The dipole magnet is positioned between the Trigger Tracker and the three downstream tracking stations. It was designed with an integrated magnetic field of 4 T·m, operating over a track length of 10 meters. The magnetic field bends the trajectories of charged particles within the tracking stations, allowing momentum to be measured based on the relationship between the deflection angle and the field strength. Outside the tracking stations, the magnetic field remains below 2 mT to avoid interference with particle identification in the RICH detector.

3.1.3 Ring Imaging Cherenkov

There are two Ring Imaging Cherenkov (RICH) detectors: one located on the left side of the magnet and the other on the right. They are filled with a material such that, when a particle passes through, a cone of Cherenkov radiation is emitted with a characteristic opening angle [32]

$$\cos\theta_c = \frac{1}{n\beta}. \tag{3.1}$$

Here, β is the particle's velocity divided by the speed of light in vacuum, c, and n is the refractive index of the traversed material. When the particle's velocity exceeds the speed of light in the medium, Cherenkov radiation is emitted, i.e., when β is greater than a threshold value equal to $1/n$. The mass of the particle can be determined from its momentum - obtained from the curvature of its trajectory - and the Cherenkov angle [32]

$$m = \frac{p}{c}\sqrt{n^2\cos^2\theta_c - 1}. \tag{3.2}$$

RICH1 is located upstream of the magnet, between the VELO and TT stations. It is filled with an aerogel solid radiator and a C_4F_{10} gas radiator, allowing particle identification in the momentum range of 1 to 60 GeV/c. RICH2 is positioned downstream of the magnet, between the last T-station and the first muon station (M1). It contains a CF_4 gas radiator and covers a momentum range from 15 to 100 GeV/c. The following figure (see Fig. 3.4) shows the relationship between Cherenkov angle and momentum for the three radiator materials [32].

3.1.4 SPD/PS detector

Before the electromagnetic calorimeter (ECAL) and hadronic calorimeter (HCAL), there is a double detector constructed from three parts: the Scintillator Pad Detector (SPD), a 2.5 radiation-length lead wall, and the Preshower (PS). The SPD/PS system aims to provide the calorimeter with good background rejection and acceptable efficiency in photon detection, with sufficient precision to allow the reconstruction of B-decay channels containing a prompt photon or π_0, as well as for electron identification. The SPD detector distinguishes electrons from photons by identifying charged particles, while the Preshower detector identifies electromagnetic particles [33].

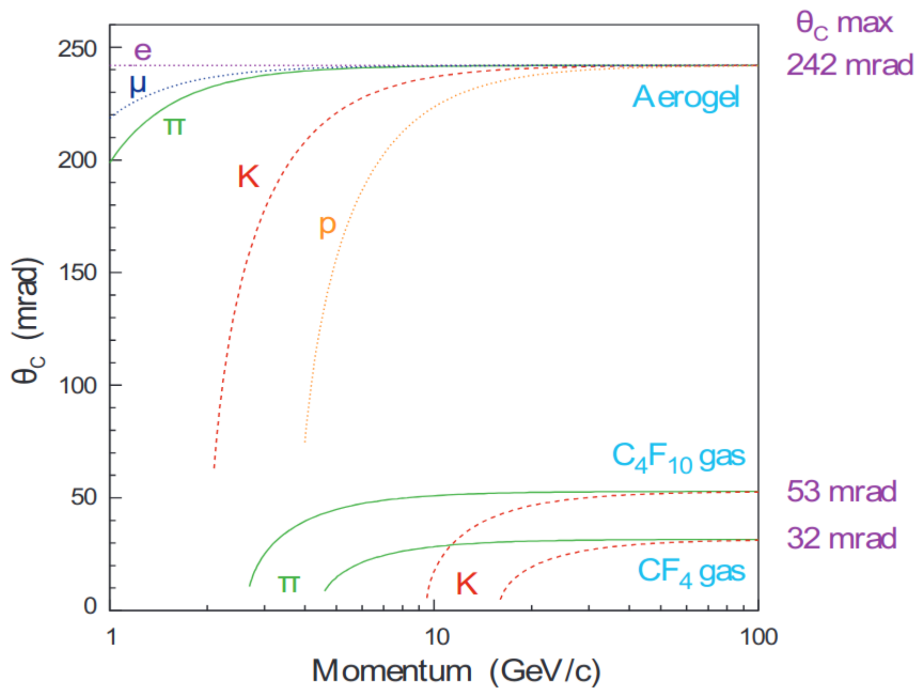

Figure 3.4: Cherenkov angle versus particle momentum for the RICH radiators. Extracted from [23].

3.1.5 Calorimeter

The calorimeter is used to measure the energy loss of particles by absorbing their energy through interactions with the detector material. First comes the ECAL, followed by the HCAL. A scintillator pad detector, located in front of the ECAL, is used to detect charged particles and is placed directly in front of a preshower detector. The ECAL is constructed using a scintillator/lead structure and is segmented into three sections, each with appropriately sized cells to account for the decreasing hit density with increasing distance from the beam pipe. The HCAL consists of iron/scintillator tiles arranged parallel to the beam pipe. The scintillation light is detected by photomultiplier tubes (PMTs) and transmitted through optical fibers [34].

3.1.6 Muon System

The muon system [35] is capable of sending binary information to the data acquisition (DAQ) system and to the hardware computations of the muon trigger

(L0MU). Together with the calorimeter trigger, it forms the so-called first-level trigger. The muon system consists of five stations, M1–M5, positioned along the beam pipe. Station M1 is located between RICH2 and the calorimeter to improve the p_T measurement in the trigger and to avoid hits caused by multiple scattering in the absorber materials. The stations are designed with 276 multi-wire proportional chambers, excluding the inner part of the first station - subject to the highest radiation - which is composed of 12 Gas Electron Multiplier detectors. The L0MU trigger performs muon track reconstruction, requiring hits in all five stations and measuring the transverse momentum of the tracks.

3.1.7 Trigger

In Run 2, where the data used in this study was taken, the event rate was 40 MHz, but not all events are of interest. Therefore, the trigger system was used to reduce this rate to ≈ 12 kHz in Run 2 [36], which could then be stored. The trigger system had three different levels; as events progress through these stages, the reconstruction becomes increasingly sophisticated. The trigger workflow is illustrated in the following figure 3.5.

The first stage of the trigger, L0, is a hardware system that partially reconstructs the event based primarily on information from the calorimeters and the muon system. The input rate to L0 is 40 MHz [38]. The L0 level mainly performs selection either per particle or based on overall event multiplicity, the latter primarily measured by the occupancy of the SPD (nSPDHits). At this stage, the preshower (PS) detector helps distinguish photons from electrons. Events passing through L0 are sent to a CPU farm that executes the High Level Trigger (HLT), which is divided into two stages: HLT1 and HLT2. HLT1 reconstructs tracks of charged particles that traverse the entire detector, known as long tracks. These tracks are used to reconstruct the primary vertex (PV) and secondary vertices from particle decays. The output rate from HLT1 is approximately 100 kHz. HLT2 processes events stored in

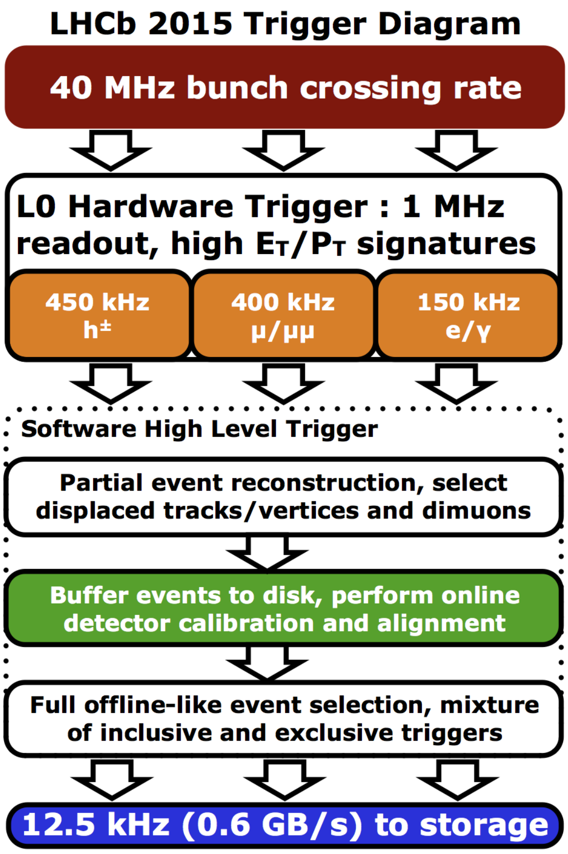

Figure 3.5: Diagram of the trigger system during Run 2. Extracted from [37].

the disk buffer, further reducing the output rate, and also performs detector calibration and alignment for the next run. After this, the reconstruction of the events is similar to that used in the offline criteria.

After the trigger selects the interesting events, they are stored for later analysis in a process known as offline analysis. Before this offline step, the data typically undergoes a process called a Stripping campaign, which performs a refined selection according to specific physics channels of interest. In Run 2, a new technique called Turbo [39] was introduced to allow certain event selections to be fully processed at the trigger level. This is particularly useful for analyses with very high event rates, as it reduces the need for extensive offline processing and storage. Additionally, a small fraction of the trigger bandwidth is allocated to a stream called TurCal, which operates similarly to Turbo but is specifically designed for calibration purposes.

3.1.8 Low multiplicity triggers

The low multiplicity[1] triggers select events with a small number of particles in the final state, i.e., events with few reconstructed tracks. Low multiplicity triggers are useful for selecting rare and clean events, such as CEP with one or two particles in the final state, heavy particle decays into two leptons (e.g., $\psi(2S) \to \mu^+\mu^-$), or exotic states with few decay products. They help reject events with characteristics of typical hadronic collisions by discarding events with high multiplicity. Since millions of collisions occur per second at the LHC, low multiplicity triggers help retain only the interesting events, saving both disk space and analysis time.

The LHCb trigger system is divided into two levels: the hardware trigger (L0), which uses fast signals from subdetectors (such as calorimeters and muon chambers) to make rapid decisions; and the software trigger, split into HLT1 and HLT2, which perform partial and full event reconstruction and apply selection criteria such as number of tracks, transverse momentum of particles, invariant mass, and event topology. Low multiplicity triggers are mainly employed at the HLT stage, where it is possible to reconstruct the number of particles in the event. For example, in this analysis, there are four tracks in the final state, low activity in the HeRSCheL detector, a pair of muons within the mass window of the $\psi(2S)$ resonance, and a pair of kaons within the mass window of the ϕ resonance - with no other hadronic activity observed.

3.1.9 Herschel

The LHCb experiment started its data-taking in 2010 during Run 1, while the HeRSCheL detector was installed and commissioned in 2015, at the beginning of Run 2. The HeRSCheL detector (High Rapidity Shower Counters for LHCb), present in the LHCb experiment, is primarily used to detect activity in high pseudorapidity regions, i.e., in the forward regions relative to the center of the detector. It is

[1]Multiplicity refers to the number of charged particles - e.g., muons, pions, protons, etc. - detected in an event.

mainly used to identify whether an event is a CEP or not. In a CEP process, a final state is produced in the central region of the detector, such as $\psi(2S)\phi$, and no other particles are produced - the protons may remain intact or break up. To confirm that the event is truly exclusive, it is necessary to verify that there is no extra activity in the detectors - especially in the blind regions of LHCb. To achieve this, HeRSCheL was positioned in such a way that it monitors the regions with $5 < |\eta| < 10$. Non-exclusive events produce particles in all directions. If HeRSCheL detects signals, it is an indication that the event is not exclusive and can be discarded. This improves the purity of the sample.

HeRSCheL has five plates positioned at different distances relative to the interaction point (see figure 3.6); three of these are backward stations, known as B stations, located in the negative z direction, and two are forward stations, known as F stations, located in the positive z direction.

The B0, B1, and B2 stations are located at approximately $z \approx -7.5$ m, $z \approx -19.5$ m, and $z \approx -114$ m, respectively, while the F1 and F2 stations are positioned at approximately $z \approx 20$ m and $z \approx 114$ m. The B2 and F2 plates are near the point where the vacuum splits into two separate chambers, one for each beam.

The plates are made of plastic scintillator with outer dimensions of 600 mm $\times$ 600 mm, centered around the beam pipe. Due to the layout of the vacuum chamber, the stations have different inner openings. The B0, B1, and F1 stations have circular holes with diameters of 47 mm (B0, B1) and 61 mm (F1), respectively. For B2 and F2, the half-widths are 115 mm (due to the size of the vacuum chambers) horizontally and 54 mm vertically [40].

Each plane has four counters, so the five planes of HeRSCheL have a total of twenty counters. The main method to combine the activity from all HeRSCheL detectors is through a quantity called χ^2, denoted as ϵ_{HRC}. When this quantity is close to zero, it indicates almost no activity in the HeRSCheL counters, which corresponds to the CEP process. Conversely, higher values of this quantity indicate

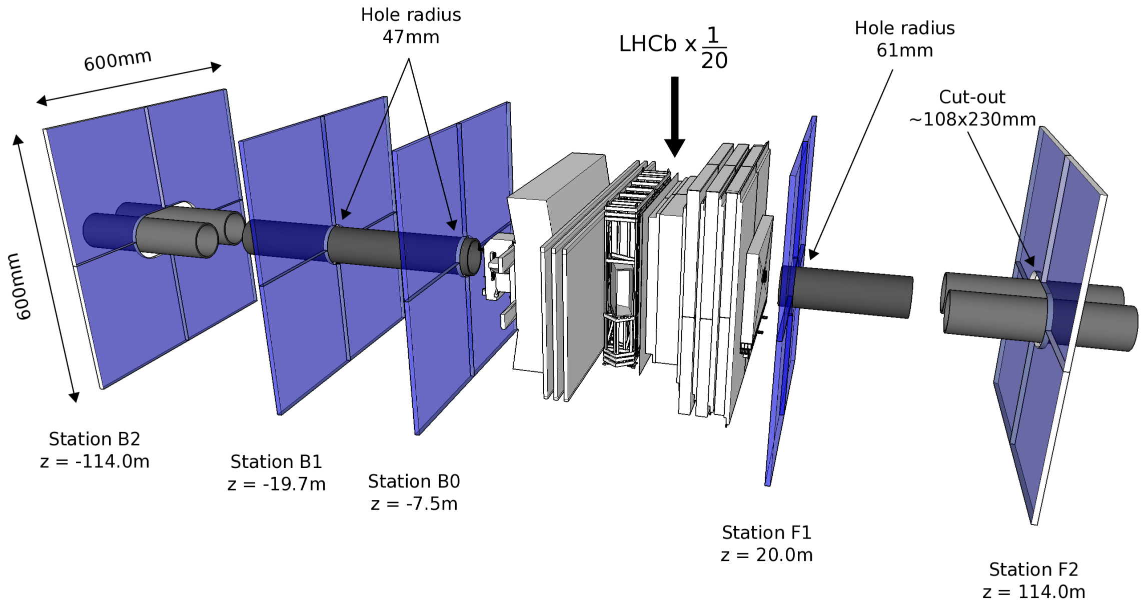

Figure 3.6: Schematic of HeRSCheL. Extracted from [40].

increased activity in the counters, corresponding to non-CEP processes [40].

3.2 Data processing framework

There is a larger project called Gaudi that encompasses the software used by LHCb to process data [41]. This framework was developed for use at LHCb and integrates different applications. The main ones are:

- GAUSS [42]: A simulation framework that brings together different particle decay generators and simulates their interaction with the detector.

- BOOLE [43]: Completes the simulation stage by reproducing the detector's electronic response. The output is then processed by BRUNEL, just like real data.

- MOORE [43]: Defines and applies the trigger algorithms during the software phase.

- BRUNEL [44]: Performs the reconstruction of the events.

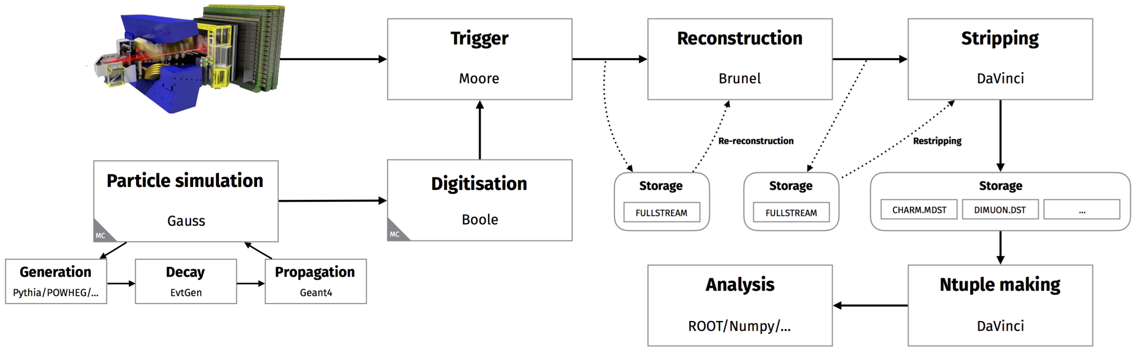

Figure 3.7: Data flow in LHCb. Extracted from [46].

- DaVinci [45]: Handles data analysis, working with the reconstructed content to select and analyze the kinematics of the particles.

In Fig. 3.7, there is a schematization of the data processing flow including the simulation applications. The information read is saved in RAW files.

BRUNEL is responsible for reading this data, reconstructing the events, and saving them in Data Summary Tape (DST) files, which integrated both the raw events and the content from the reconstruction phase. The data then goes through a process called "stripping", in order to make it more accessible to the final user by reducing the file size. There are many stripping lines, each one corresponding to a specific physical process. After that, the stripped data can be further divided into streams, which are organized according to more specific physics processes. The stripped data is stored in DST or micro-DST files with reduced size, making the analysis more accessible and faster.

3.3 Simulation

Besides the real data, simulated samples are also generated to analyze the detector response and to compare experimental results with theoretical predictions. The simulation provides an idea of what happens in real life. For example, simulated events reproduce the particles produced in the LHCb environment in such a way that it is possible to model the signal decays. The production of all particles in the simulation process allows for the estimation of quantities such as the detector efficiency. The simulation production [47] can be divided into three phases.

Event Generation: The production of particles in collision events such as pp or pPb is simulated using theoretical models. There are multiple generators available, such as Pythia [48], used to simulate pp collisions, or EPOS [49] and StarLight for other collision types..

Decay Simulation: The resonance $\psi(2S)$ can decay into different final-state particles, each with a certain probability. This can also occur with other unstable particles. The software responsible for simulating these decays is called EVT-GEN [50].

Propagation through the detector: After the particles are produced, they propagate and interact with the detector material. This process is simulated using the GEANT4 [51] software.

The process selection for the simulation is the same as for the real data. The trigger selection decides which simulated events must be stored or rejected, in accordance with the selection criteria. The particles generated by the simulation, before interacting with the detector or decaying, are saved separately. This allows for the estimation of selection efficiencies and helps to better understand the experimental effects and how they are connected to measured quantities, which contributes to a clearer understanding of the detector effects in the final analysis.

Chapter 4

$\psi(2S)\phi$ analysis results

4.1 Objective

The $\psi(2S)\phi$ CEP cross-section is calculated in proton-proton collisions at $\sqrt{s}$ = 13 TeV. CEP is a diffractive process in which protons interact quasi-elastically, resulting in the production of an exclusive system X. The interaction is mediated by propagators such as photons and pomerons. Due to the distinct features of CEP, it can be studied experimentally with reduced background noise, allowing for a more precise understanding of the production mechanism.

Studies of CEP within the LHCb detector can enhance our understanding of the pomeron, improve predictions from perturbative QCD, and contribute to constraining gluon parton distribution functions (PDFs) at low momentum fractions. The LHCb collaboration has already investigated CEP involving charmonia and muon pairs [52].

The analysis is based on data collected at a center-of-mass energy of 13 TeV during Run 2 at LHCb, corresponding to an integrated luminosity of 1.73 fb^{-1}. The reconstruction was performed using $\psi(2S)$ decays into muon pairs and ϕ mesons decaying into kaon pairs, within the pseudorapidity range $2 < \eta < 5$ and a transverse momentum threshold of $p_T > 200$ MeV. 40 candidate events are selected. The measured cross-section is found to be

$$\sigma_{\psi(2S)\phi} = 0.0723 \pm 0.0117 \text{ (stat.) pb.} \tag{4.1}$$

The cross-section is calculated according to the following expression:

$$\sigma = \frac{p \cdot N}{\bar{\epsilon} \cdot \mathcal{L}_{eff}} \tag{4.2}$$

here, p represents the sample purity, N is the number of selected events, $\bar{\epsilon}$ denotes the selection efficiency, and $\mathcal{L}_{\text{eff}}$ refers to the effective integrated luminosity.

4.2 Data sample characteristic

The data were collected from 2016 to 2018 during Run 2 at the LHC, with a center-of-mass energy of 13 TeV. The integrated luminosity (1747 ± 34.94) pb^{-1} was calculated in Ref. [15] according to the method described in [53].

The $\mu\mu$ decay channel of the $\psi(2S)$ was chosen over the ee channel due to the frequent misidentification of electron pairs, although electrons can be identified by LHCb. Furthermore, electrons lose significant energy through bremsstrahlung, resulting in poorer mass resolution [15].

The muon Particle ID (PID) and trigger efficiencies are obtained from a separate study that used additional samples based on low-multiplicity J/ψ production. The same approach is applied to the kaon PID efficiency, which is computed using a low-multiplicity ϕ production sample. Furthermore, the $\mathcal{L}_{\text{eff}}$ for CEP is derived from a NoBias[1] sample.

4.3 Luminosity adjustment

Only bunches with proton-proton interactions are retained due to the requirement of a threshold of four tracks. As a result, only a fraction $f_{\mathcal{L}}$ of the integrated luminosity $\mathcal{L}_{int}$ is actually usable. Consequently, the effective integrated luminosity can be determined as follows [15]:

$$\mathcal{L}_{\text{int}}^{\text{eff}} = f_{\mathcal{L}} \cdot \mathcal{L}_{int}. \tag{4.3}$$

[1] It refers to data taken randomly without any additional criteria.

This effective luminosity is calculated following the methods described in Ref. [53]. The luminosity must account for pile-up vetoes[2] and the bias due to variations in the number of pp collisions per bunch crossing. Thus, the $f_{\mathcal{L}}$ factor is calculated taking these effects into account.

At this point, it is important to specify what constitutes a visible event in relation to the average number of visible interactions per bunch crossing μ. According to the LHCb Luminosity Group, a visible event is defined as one with a reconstructable primary vertex within the luminous region, specifically at $z = (0 \pm 50\text{mm})$. However, reconstructing the primary vertex requires at least five VELO tracks. Since this analysis involves only four tracks, that definition is not applicable [15].

In this case, the veto is applied based on the number of VELO tracks (nVeloTracks) rather than on additional reconstructed primary vertices. Therefore, the definition must be adjusted to fit this approach [15]

$$\text{Visible} = (\text{nVeloTracks} > 0). \tag{4.4}$$

Therefore, the correct effective integrated luminosity, considering the above definition and the fraction of empty events, f_0, which is calculated per polarity using the NoBias sample., is

$$\mathcal{L}_{\text{int}}^{\text{eff(corr)}} = f_0 \cdot \mathcal{L}_{\text{int}} \tag{4.5}$$

This equation does not consider the effects discussed in [53], but incorporates them as systematic uncertainties. The uncertainty in $\mathcal{L}_{\text{int}}^{\text{eff(corr)}}$ is evaluated using the following equation [15]:

$$\sigma_{\mathcal{L}_{\text{int}}^{\text{eff(corr)}}} = \mathcal{L}_{\text{int}}^{\text{eff(corr)}} \cdot \sqrt{\left(\frac{\sigma_{f_0}}{f_0}\right)^2 + \left(\frac{\sigma_{\mathcal{L}_{int}}}{\mathcal{L}_{int}}\right)^2 + (1\%)^2} \tag{4.6}$$

where $\sigma_{\mathcal{L}_{\text{int}}^{\text{eff}}}$ denotes the uncertainty in the uncorrected effective luminosity, and σ_{f_0} represents the statistical error on f_0. The first term inside the square root is negligible compared to the second, which is dominant. This is because $\frac{\sigma_{f_0}}{f_0}$ is approximately

[2]The method used to identify and reject results affected by multiple interactions.

1% of $\frac{\sigma_{\mathcal{L}^{\text{eff}}_{\text{int}}}}{\mathcal{L}^{\text{eff}}_{\text{int}}}$, while the uncertainty in the uncorrected luminosity is about 3% [15]. The 1% accounts for effects discussed in reference [53]. Although luminosity-related effects, such as the spread of the average number of pp interactions per bunch crossing and beam-gas corrections, can introduce a bias of about 1% in the effective luminosity for CEP analyses, these corrections are not included in the present work.

4.4 $J/\psi\phi$ simulation sample

A simulated sample of J/ψ from Ref. [15] was used to compute tracking efficiencies, acceptances, and mass resolution. This sample was privately generated by modifying the decay process in SuperChic3 [54] from $J/\psi(\to \mu^+\mu^-)J/\psi(\to \mu^+\mu^-)$ to $J/\psi(\to \mu^+\mu^-)\phi(\to K^+K^-)$ and by adjusting the mass of one of the J/ψ mesons. The events generated by SuperChic3 were processed through the full simulation chain, including Gauss v49r15p1, Boole v30r4, Moore v25r4, and Brunel v50r5. The framework also incorporates EvtGen for particle decays and Geant4 for simulating particle interactions with the detector.

4.5 J/ψ simulation sample

The J/ψ simulation sample used in [15] was employed to compute the sample purity and the efficiency of the mass requirements. This simulation was generated using the decay $J/\psi(\to \mu^+\mu^-)$ with SuperChic2, rather than SuperChic3, because the sample was already centrally produced within LHCb. Although SuperChic3 includes enhancements specific to heavy-ion interactions, these are not relevant for this analysis.

4.6 Event Selection

To improve the signal and reduce background noise, events that are consistent with $\psi(2S)\phi$ must be selected, while those that are not should be excluded. This is achieved using the trigger system and by setting thresholds on the variable properties of the particles present in the event.

4.6.1 Trigger system

It is unfeasible to store all events that occur in LHCb, so a trigger system is implemented to select only the most relevant ones. The trigger system is divided into two parts: L0 and HLT. L0 operates with hardware components, verifying raw kinematic information. In Run 2, the HLT is further divided into two stages: HLT1 and HLT2. HLT1 performs partial reconstruction, while HLT2 performs full reconstruction. When an event passes through all required stages, it is said to satisfy a trigger line.

In this study, the trigger line described in Ref. [15] was used. The trigger line includes the following requirements: one of the muons must have $p_T > 200$ MeV and fewer than 20 hits in the SPD, as part of the L0 trigger line `L0Muon,lowMult`.

On the other hand, HLT1 has the following requirements for data taken before 2016 (corresponding to run numbers less than 178960): fewer than 100 reconstructed VELO tracks and fewer than 100 hits in the SPD. This is referred to as the trigger line `HLT1LowMultVeloCut_Leptons`.

After 2016, the HLT1 requirements were updated to include: fewer than 10 reconstructed VELO tracks, fewer than 100 hits in the SPD, a track identified as a muon with $p_T > 500$ MeV/c, and a χ^2 per degree of freedom must be less than 5. This quantity, χ^2/ndf, is computed by matching the L0 tracks to the HLT1 VELO track candidates [55]. This is referred to as the trigger line `HLT1LowMultMuon`. After 2016, `HLT1LowMultVeloCut_Leptons` was replaced by `HLT1LowMultMuon`.

HLT2 has the additional requirements of fewer than 8 reconstructed VELO tracks, identification of a muon with $p_T > 400$ MeV/c, and no backward tracks, as part of the `HLT2LowMultMuon` trigger line (see table 4.1).

Level	Trigger Line	Requirements
L0	`L0Muon,lowMult`	$N_{SPD} < 20$ Muon with $p_T > 200$ MeV/c
HLT1 (< 178960)	`HLT1LowMultVeloCut_Leptons`	$N_{SPD} < 100$ nVeloTracks < 100
HLT1 (≥ 178960)	`HLT1LowMultMuon`	$N_{SPD} < 100$ nVeloTracks < 10 Muon with $p_T > 500$ MeV/c χ^2/ndf < 5
HLT2	`HLT2LowMultMuon`	nVeloTracks < 8 nBackTracks < 1 Muon with $p_T > 400$ MeV/c

Table 4.1: The triggers criteria, where the HLT1 depend on the data taking period. Table extracted from [15].

4.6.2 Offline selection

There is an initial step involving a trigger system that significantly reduces the data volume, known as online selection. After this, offline selection is performed, which includes further analysis and refinement of the data. During this stage, cuts are applied to events involving the decay of the $\psi(2S)$ into a muon pair and the decay of the ϕ into a kaon pair, as can be seen in the following lines[3].

- Pseudorapidity: can also be understood in terms of acceptance and requires the presence of at least four tracks within the range $2 < \eta < 5$.

- Exclusivity: No backward tracks are allowed. Exactly four VELO and long tracks must be selected.

- p_T: Each of the four tracks must have $p_T > 200$ MeV/c.

- TOS and Muon ID: The trigger conditions require selecting four tracks, two of which must be identified as muons. Additionally, one of these muons must pass through all trigger stages (L0, HLT1, and HLT2). This requirement is known as TOS (Triggered On Signal) and applies to all trigger stages.

[3] The selection cuts were optimized by Ref. [15].

- Kaon ID: The tracks forming the di-kaon pair must satisfy the condition PIDK > 0.

- The masses of the reconstructed $\mu\mu$ and KK systems must satisfy the criteria: $3566 < M_{\mu\mu}/\mathrm{MeV} < 3806$ for the $\mu\mu$ system, and $1005 < M_{KK}/\mathrm{MeV} < 1035$ for the KK system.

The TOS particles are identified using an algorithm called TupleToolTISTOS, which retains particles that triggered the event. During the offline analysis, these stored trigger signals are compared with the selected candidates to ensure that the candidates fired the trigger. TupleToolTISTOS performs this comparison, and if the overlap is 70% or greater, the candidates are considered a match. This method is especially effective for determining whether a muon is TOS (Triggered On Signal) and, using this information, calculating the trigger efficiency. To facilitate particle identification, discriminating variables such as IsMuon and PIDK are applied. The PIDK variable compares the likelihood of a particle being a kaon versus a pion; a positive PIDK value indicates a higher probability that the particle is a kaon. The muonID is a Boolean variable based on muon system information; if true, it indicates that the track has passed through the muon stations [15].

Figures 4.1-4.11 show the distributions obtained from the data, which correspond to a total of 40 selected events. The invariant mass distributions for K^+K^- and $\mu^+\mu^-$ are shown in Figures 4.1a and 4.1b. The invariant mass distribution for $K^+K^-\mu^+\mu^-$ and the transverse momentum squared distributions of K^+K^- and $\mu^+\mu^-$ are shown in Figures 4.2a and 4.2b, respectively. The transverse momentum distributions of K^- and K^+, as well as of μ^- and μ^+, are presented in Figures 4.3a and 4.3b. The ϕ distributions of K^- and K^+, and of μ^- and μ^+, are shown in Figures 4.4a and 4.4b, while their η distributions are displayed in Figures 4.5a and 4.5b. The K^+K^- mass versus transverse momentum squared and the transverse momentum squared of K^+K^- versus that of $\mu^+\mu^-$ are shown in Figures 4.6a and 4.6b.

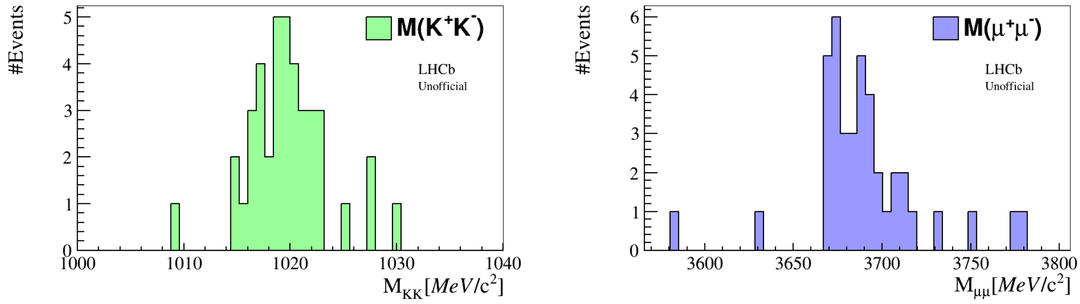

(a) Distribution of the K^+K^- invariant mass. (b) Distribution of the $\mu^+\mu^-$ invariant mass.

Figure 4.1: Distribution of the invariant mass.

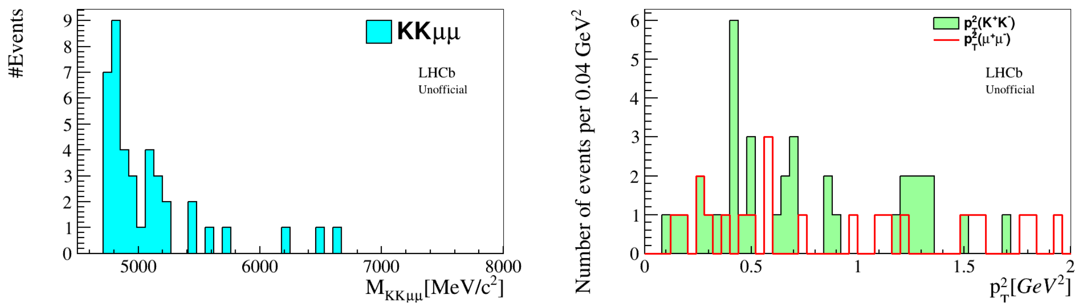

(a) Distribution of the $K^+K^-\mu^+\mu^-$ invariant mass. (b) Distribution of the p_T^2 of the K^+K^- system versus the p_T^2 of the $\mu^+\mu^-$ system.

Figure 4.2: Distribution of the $K^+K^-\mu^+\mu^-$ invariant mass (left) and distribution of the p_T^2 of the K^+K^- system versus the p_T^2 of the $\mu^+\mu^-$ system (right).

The K^+K^- versus $\mu^+\mu^-$ invariant mass and the photon multiplicity are shown in Figures 4.7a and 4.7b.

The mass distributions of $\mu^+\mu^-K^+$ and $\mu^+\mu^-K^-$ are shown in Figures 4.8a and 4.8b, respectively. The corresponding transverse momentum distributions are presented in Figures 4.9a and 4.9b, the ϕ distributions in Figures 4.10a and 4.10b, and the η distributions in Figures 4.11a and 4.11b.

4.7 Purity Determination

It is common for events studied in nature to have similar occurrences that are not of interest, referred to as backgrounds, and this principle also applies in particle physics. In this analysis, certain particles may mimic the signal; for example, an electron can be misidentified as a kaon, or the mass of muon pairs may fall within

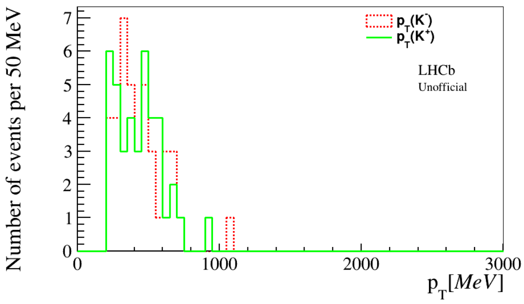

(a) Distribution of the K^+K^- p_T.

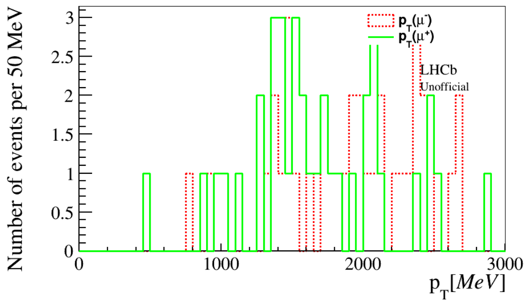

(b) Distribution of the $\mu^+\mu^-$ transverse momentum (p_T)

Figure 4.3: Distribution of the K^+K^- and $\mu^+\mu^-$ p_T.

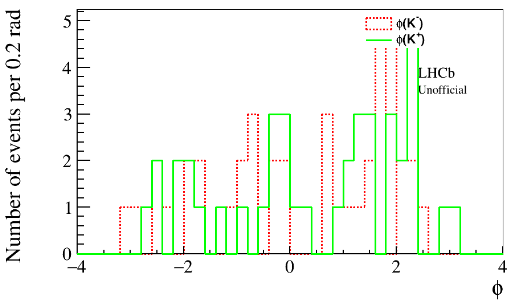

(a) Distribution of the K^+K^- ϕ.

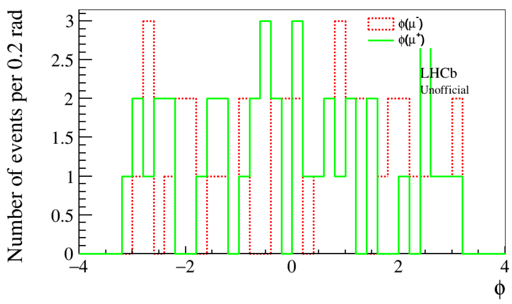

(b) Distribution of the $\mu^+\mu^-$ ϕ.

Figure 4.4: Distribution of the K^+K^- and $\mu^+\mu^-$ ϕ.

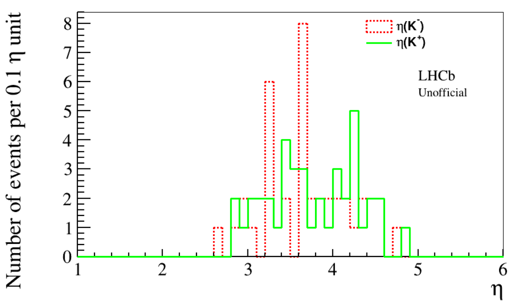

(a) Distribution of the K^+K^- η.

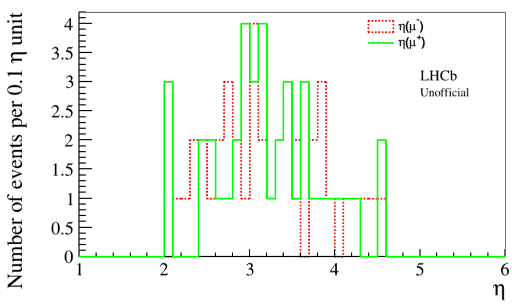

(b) Distribution of the $\mu^+\mu^-$ ϕ.

Figure 4.5: Distribution of the K^+K^- and $\mu^+\mu^-$ η.

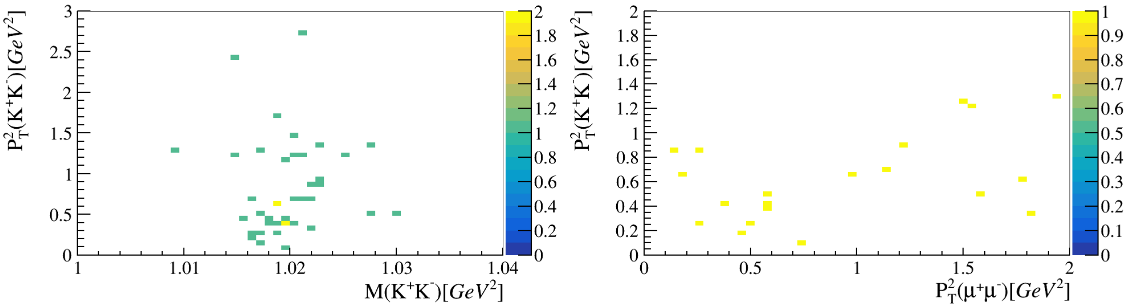

(a) Distribution of the K^+K^- invariant mass versus K^+K^- p_T^2.

(b) Distribution of the $\mu^+\mu^-$ p_T^2 versus K^+K^- p_T^2.

Figure 4.6: 2D distributions of the K^+K^- invariant mass versus p_T^2 (left), and the K^+K^- p_T^2 versus the $\mu^+\mu^-$ p_T^2 (right). These plots provide insights into the kinematic correlations and transverse momentum balance in $\psi(2S)\phi$ Central Exclusive Production events.

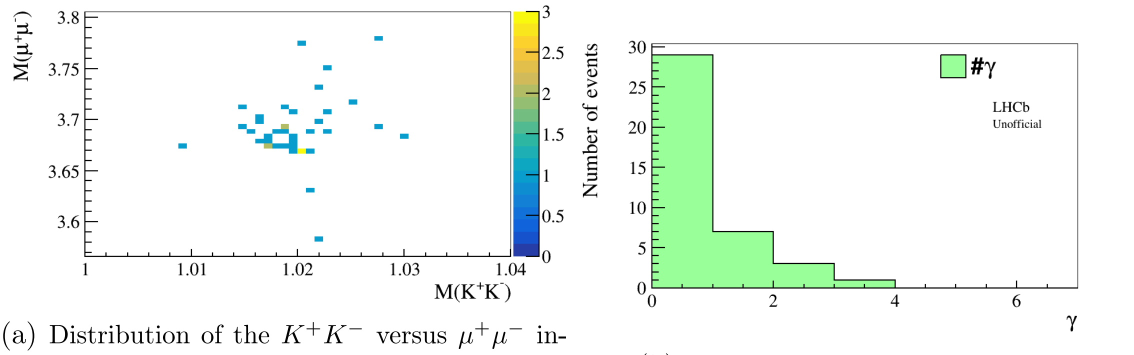

(a) Distribution of the K^+K^- versus $\mu^+\mu^-$ invariant mass.

(b) Photon multiplicity distribution.

Figure 4.7: Distribution of the K^+K^- versus $\mu^+\mu^-$ invariant mass and photon multiplicity.

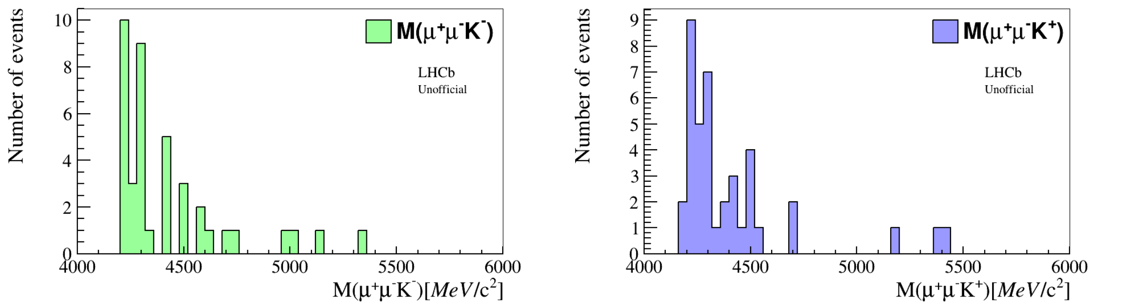

(a) Distribution of the invariant mass of the $\mu^+\mu^-K^-$ system.

(b) Distribution of the invariant mass of the $\mu^+\mu^-K^+$ system.

Figure 4.8: Distribution of the invariant mass of the $\mu^+\mu^-K^-$ and $\mu^+\mu^-K^+$ system.

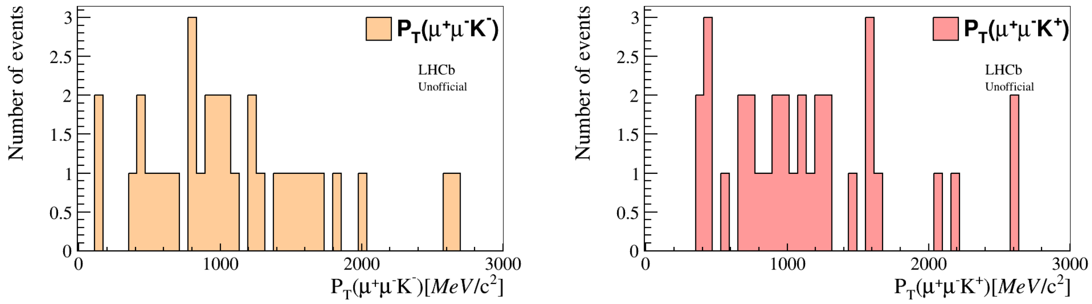

(a) Distribution of the p_T of the $\mu^+\mu^-K^-$ system.

(b) Distribution of the p_T of the $\mu^+\mu^-K^+$ system.

Figure 4.9: Distribution of the p_T of the $\mu^+\mu^-K^-$ and $\mu^+\mu^-K^+$ system.

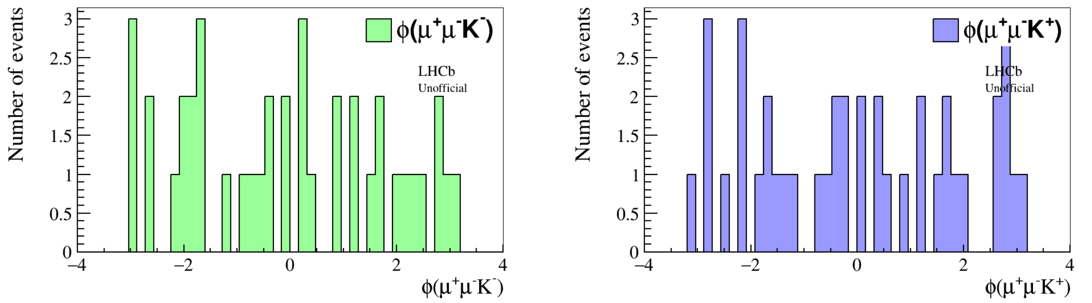

(a) Distribution of the ϕ of the $\mu^+\mu^-K^-$ system.

(b) Distribution of the ϕ of the $\mu^+\mu^-K^+$ system.

Figure 4.10: Distribution of the ϕ of the $\mu^+\mu^-K^-$ and $\mu^+\mu^-K^+$ system.

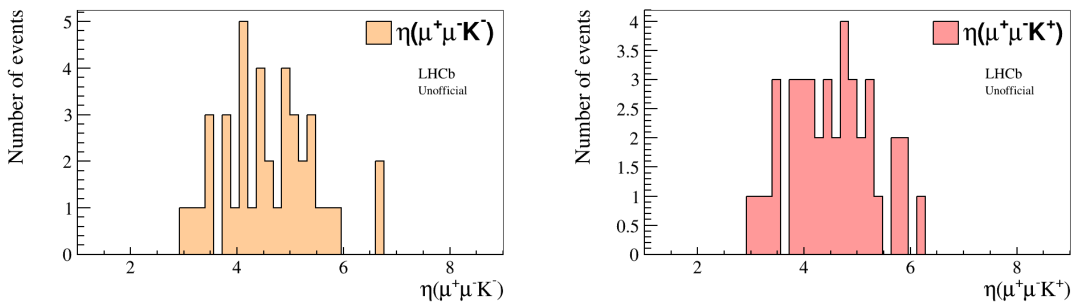

(a) Distribution of the η of the $\mu^+\mu^-K^-$ system.

(b) Distribution of the η of the $\mu^+\mu^-K^+$ system.

Figure 4.11: Distribution of the η of the $\mu^+\mu^-K^-$ and $\mu^+\mu^-K^+$ system.

the $\psi(2S)$ mass window without actually being a $\psi(2S)$. Therefore, it is necessary to calculate the sample purity to quantify the proportion of true signal events in the sample.

The non-resonant background was calculated using a simultaneous (2D) unbinned maximum likelihood fit applied to the mass distributions of the $\psi(2S)$ and ϕ over extended mass ranges: $3566 < M_{\mu\mu}, (\mathrm{MeV}/c^2) < 3806$ and $1005 < M_{KK}, (\mathrm{MeV}/c^2) < 1035$.

For the $\mu\mu$ mass spectrum, the $\psi(2S)$ signal is modeled using a Gaussian function. In contrast, the J/ψ signal is described by a Double-Sided Crystal Ball function, implemented via the RooCrystalBall package in ROOT v6.24.08. The non-resonant background is fitted using an exponential distribution. Although it is possible to model the $\psi(2S)$ signal with a Double-Sided Crystal Ball function - as done for the J/ψ - this does not yield a significant improvement due to the limited data available. Therefore, a Gaussian function is preferred for modeling the $\psi(2S)$ signal, as it simplifies the parameter-setting process. The tail parameters of the Double-Sided Crystal Ball function are fixed using simulation, based on the sample shown in Sec. 4.5.

The KK mass spectrum includes a non-resonant background, which is modeled using a uniform function. However, this is not physically accurate, as the background is expected to decay exponentially at higher masses. Nevertheless the presence of misidentified electrons further complicates the background modeling. Thus, a uniform background was chosen for simplicity and because it is sufficient to model the background within the fitting range. The ϕ signal is modeled using a modified Voigt profile, which combines a relativistic Breit-Wigner function with a mass-dependent width, convoluted with a Gaussian to account for resolution effects.

A relativistic Breit-Wigner function is used to model the ϕ component

$$BW(M_{KK};\mu_\phi,\Gamma_\phi) = \frac{M_{KK}\Gamma}{(M_{KK}^2-\mu_\phi^2)^2+\mu_\phi^2\Gamma^2} \tag{4.7}$$

in this equation, μ_ϕ represents the mass of the ϕ meson, and Γ is the mass-dependent width, written as

$$\Gamma = \Gamma_\phi \frac{\mu_\phi}{M_{KK}} \left(\frac{q(M_{KK})}{q(\mu_\phi)} \right)^{2L+1} \left(\frac{F_L(M_{KK}, r_0)}{F_L(\mu_\phi, r_0)} \right)^2 \tag{4.8}$$

where Γ_ϕ is the Breit-Wigner width, $L = 1$ is the spin of the ϕ, $F_1(q, r_0) = \frac{1}{\sqrt{1+r_0^2 q^2}}$ is the Blatt-Weisskopf form factor for $L = 1$, and r_0 is the meson radius (set to 1 fm or 5.1 GeV^{-1}). The quantity $q(m) = \sqrt{\frac{m^2}{4} - M_K^2}$ is the kaon momentum in the ϕ rest frame.

The next step is to construct the modified Voigt profile by convolution of the Breit-Wigner function, $BW(M_{KK}; \mu_\phi, \Gamma_\phi)$, with a Gaussian.

$$V(M_{KK}; \mu_\phi, \sigma_\phi, \Gamma_\phi) = G(M_{KK}; 0, \sigma_\phi) * BW(M_{KK}; \mu_\phi, \Gamma_\phi) \tag{4.9}$$

The BW width Γ_ϕ is fixed according to the ϕ width from the PDG (4.249 MeV/c^2), and the Gaussian mean is set to zero, assuming no bias. The PDFs of the mass spectrum distributions are composed of partial PDFs, as previously mentioned.

$$f(M_{\mu\mu}; \mu_{J/\psi}, \sigma_{J/\psi}) = f_1' \cdot G(M_{\mu\mu}; \mu_{\psi(2S)}, \sigma_{\psi(2s)}) \tag{4.10}$$

$$+f_2' \cdot CB(M_{\mu\mu}; \mu_{J/\psi}, \sigma_{J/\psi}) + (1 - f_1' - f_2') \cdot Exp(M_{J/\psi}; c_{J/\psi}) \tag{4.11}$$

$$f(M_{KK}; \mu_\phi, \sigma_\phi) = f' \cdot V(M_{KK}; \mu_\phi, \sigma_\phi) + (1 - f') \cdot C_\phi \tag{4.12}$$

$G(M; \mu, \sigma)$ represents the gaussian modeling the signal for $\psi(2S)$, $CB(M; \mu, \sigma)$ represents the Crystall Ball function modeling the background for J/ψ, and $Exp(M; c) = e^{-c \cdot M}$ denotes the exponential background for J/ψ. Additionally, $V(M; \mu, \sigma)$ and C_ϕ represent the modified Voigt profile with Breit-Wigner mean μ and Gaussian width σ modeling the signal and uniform function modeling the background for the

ϕ, respectively. The product of these shapes results in the 2D extended model

$$f(M_{\mu\mu}, M_{KK}) = N_S \times G(M_{\mu\mu}; \mu_{\psi(2S)}, \sigma_{\psi(2S)}) \times V(M_{KK}; \mu_\phi, \sigma_\phi) \tag{4.13}$$

$$+N_B \times [f_1 \cdot G(M_{\mu\mu}; \mu_{\psi(2S)}, \sigma_{\psi(2S)}) \cdot C_\phi \tag{4.14}$$

$$+(1 - f_1) \cdot f_2 \cdot CB(M_{\mu\mu}; \mu_{J/\psi}, \sigma_{J/\psi}) \cdot C_\phi \tag{4.15}$$

$$+(1 - f_1) \cdot (1 - f_2) \cdot f_3 \cdot CB(M_{\mu\mu}; \mu_{J/\psi}, \sigma_{J/\psi}) \cdot V(M_{KK}; \mu_\phi, \sigma_\phi) \tag{4.16}$$

$$+(1 - f_1) \cdot (1 - f_2) \cdot (1 - f_3) \cdot f_4 \cdot Exp(M_{\mu\mu}; c_{J/\psi}) \cdot V(M_{KK}; \mu_\phi, \sigma_\phi) \tag{4.17}$$

$$+(1 - f_1) \cdot (1 - f_2) \cdot (1 - f_3) \cdot (1 - f_4) \cdot Exp(M_{\mu\mu}; c_{J/\psi}) \cdot C_\phi] \tag{4.18}$$

N_S corresponds to the signal yield of $\psi(2S)\phi$, and N_B corresponds to the background yield. The fraction f_1 represents the non-resonant KK background; $(1-f_1)f_2$ corresponds to the fraction of events with a resonant $\mu\mu$ pair and non-resonant KK; $(1 - f_1)(1 - f_2)f_3$ corresponds to events with both KK and $\mu\mu$ resonant pairs; $(1-f_1)(1-f_2)(1-f_3)f_4$ represents the fraction with non-resonant $\mu\mu$ and resonant KK; and finally, $(1 - f_1)(1 - f_2)(1 - f_3)(1 - f_4)$ corresponds to fully non-resonant KK and $\mu\mu$ backgrounds.

4.7.1 Purity determination

An unbinned fit is performed for both $\psi(2S)$ and ϕ, as shown in Figures 4.12 and 4.13. These figures show the projections of the fit result over the extended mass range. The results of the fit parameters are shown in the Table 4.2.

Figures 4.14a and 4.14b show the projections of the fit over the selection mass range. The resonant contribution to the background arises from events in which only one particle pair is resonant.

The fitted mass values for the J/ψ, $\psi(2S)$, and ϕ mesons are summarized in Table 4.3 and compared with the corresponding PDG averages.

The ratio of signal events to the total number of events within the selection range is referred to as the sample purity

$$p = \frac{N_S}{N_S + N_B}. \tag{4.19}$$

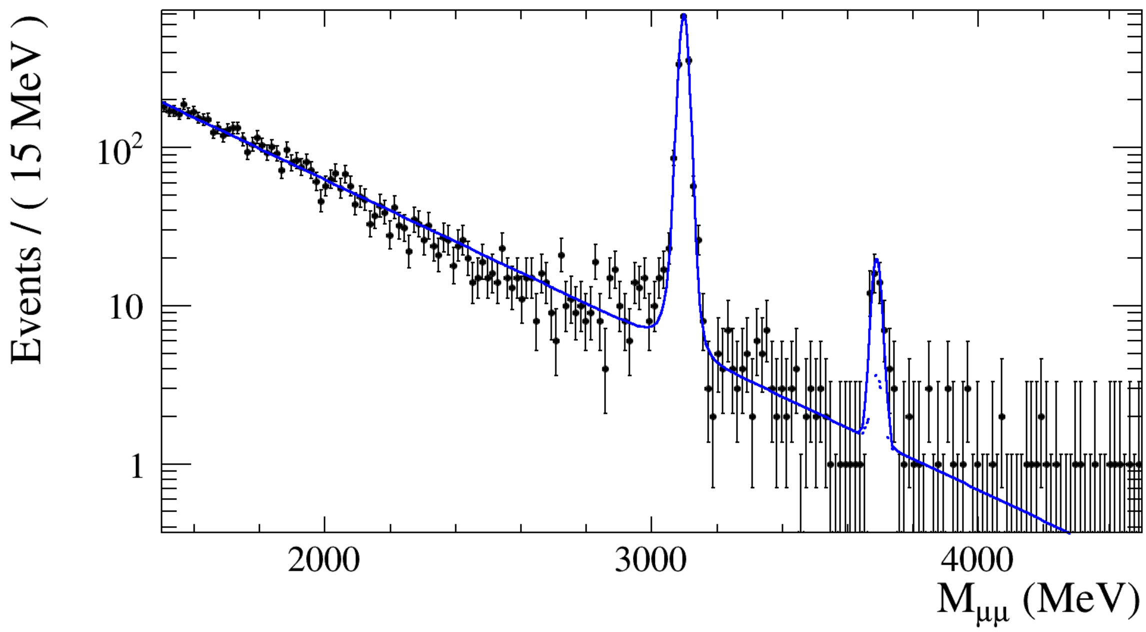

Figure 4.12: 2D unbinned fit to the $\Psi(2S)$ invariant mass spectrum over an extended range. The solid line is the full model, and the dashed line means the background, where the peak is caused by events where the pair $\mu\mu$ is background.

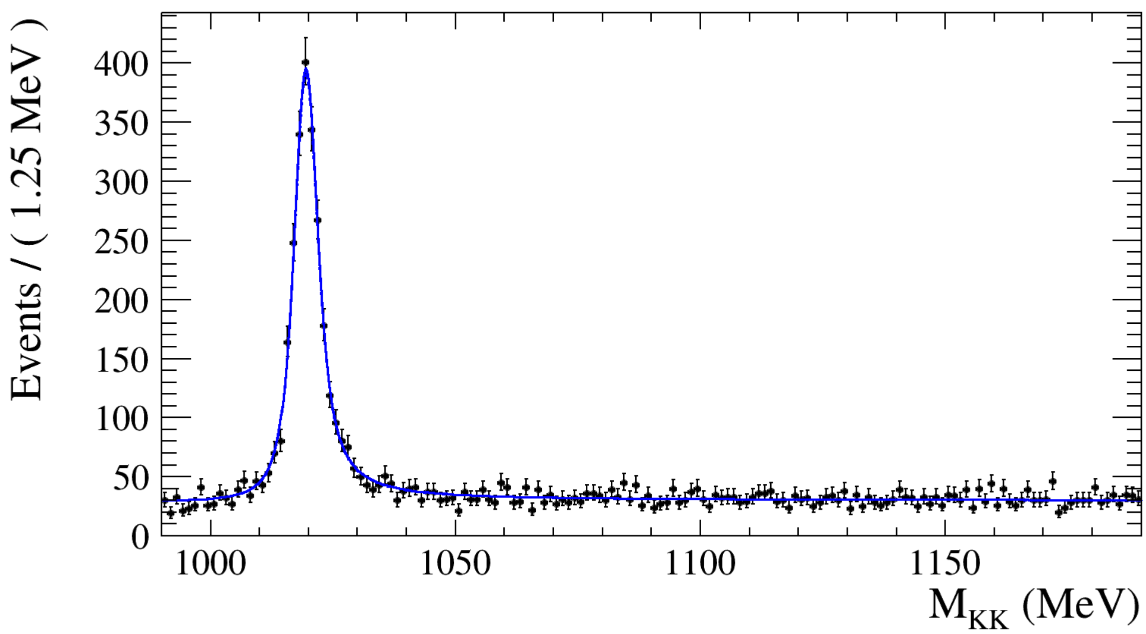

Figure 4.13: 2D unbinned fit to the ϕ invariant mass spectrum over an extended range. The solid line is the full model, and the dashed line means the background, where the peak is caused by events where the pair KK is background.

Parameters	Values
$\mu_{J/\psi}$	3099.0 ± 0.4
$\sigma_{J/\psi}$	14.7 ± 0.4
α_L	44.18 (fixed)
α_R	77.53 (fixed)
n_L	95.93 (fixed)
n_R	88.69 (fixed)
$\mu_{\psi(2S)}$	3687.7^{+3}_{-2}
$\sigma_{\psi(2S)}$	14 ± 2
$c_{J/\psi}$	88.31
μ_ϕ	1019.45 ± 0.08
σ_ϕ	1.3 ± 0.1
f_1	$0.0008^{+0.0006}_{-0.0005}$
f_2	0.061 ± 0.004
f_3	0.161 ± 0.005
f_4	0.244 ± 0.008
N_S	37^{+7}_{-6}
N_B	$(727 \pm 9) \times 10$

Table 4.2: Parameters for the simultaneous fit to the $\psi(2S)$ and ϕ. The parameters f1, f2, f3 and f4 are in the text. The parameter μ_ϕ represent the Breit-Wigner mean and σ_ϕ is the Gaussian width.

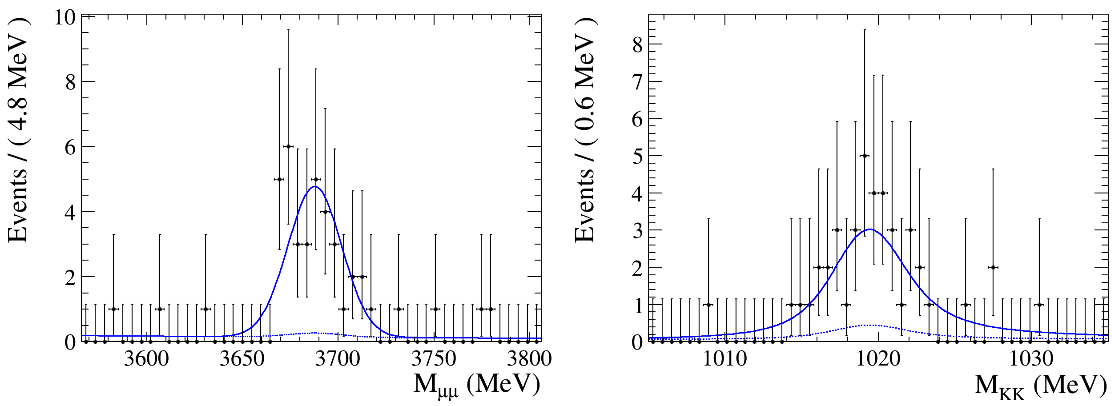

(a) $\psi(2S)$ range.

(b) ϕ range.

Figure 4.14: 2D unbinned fit of the $\psi(2S)$ and ϕ invariant mass distributions in the selection range. The solid line is the full model, and the dashed line means the background.

	Fit	PDG average
$M_{J/\psi}$ (MeV)	3099.0 ± 0.4	3096.900 ± 0.006
$M_{\psi(2S)}$ (MeV)	3687.7 ± 2.4	3686.097 ± 0.010
M_{ϕ} (MeV)	1019.45 ± 0.08	1019.460 ± 0.016

Table 4.3: Masses obtained from the fit compared with the PDG average values.

The purity is estimated to be approximately 79.72%. The systematic uncertainty is computed by propagating the fit uncertainties to the ratio, taking into account the correlations between the fit parameters.

4.8 Selection efficiencies

In Sec. 4.7, it was shown that some background events can be selected, making it important to calculate the sample purity as previously discussed. The purity, p, allows the determination of the true signal yield as $p \cdot N$, where N is the total number of events. Conversely, another important consideration is the efficiency of identifying signal events, as some signal events may be discarded. In this case, the signal yield can be quantified by the expression $\frac{N_S}{\epsilon}$, where ϵ is the total efficiency. The total efficiency for a single event is given by the factorization of all individual efficiencies considered, such as: SPD efficiency (ϵ_{SPD}), VELO efficiency (ϵ_{VELO}), reconstruction efficiency (ϵ_{rec}), muon chamber acceptance (ϵ_{muAcc}), muon PID efficiency (ϵ_{IsMuon}), trigger efficiency (ϵ_{trig}), kaon PID efficiency (ϵ_{kaonID}), and mass selection efficiency (ϵ_{mass}):

$$\epsilon = \epsilon_{SPD} \cdot \epsilon_{VELO} \cdot \epsilon_{rec} \cdot \epsilon_{muAcc} \cdot \epsilon_{IsMuon} \cdot \epsilon_{trig} \cdot \epsilon_{kaonID} \cdot \epsilon_{mass} \tag{4.20}$$

All these efficiencies were obtained from histograms used in the work of Ref. [15].

Obtained efficiencies

To measure the trigger and PID efficiencies, a data-driven method known as Tag&Probe is used. This method is useful because it does not require simulation, relying solely on data. In the case of $J/\psi \to \mu\mu$ decays, the procedure involves three steps: First, a muon is selected using strict trigger requirements to ensure it is a genuine muon (the "Tag"). Second, another track is selected as a muon candidate under looser trigger criteria (the "Probe"). Third, the invariant mass of the dimuon system is calculated, and if it matches the J/ψ mass, the Probe track is confirmed as a real muon. This method allows the efficiency to be quantified as:

$$\epsilon = \frac{N_{\text{Probe passing}}}{N_{\text{Total Probes}}}. \tag{4.21}$$

The efficiency of the SPD cut is determined based on Ref. [56]. The distribution of the number of SPD hits without any selection is modeled using both simulation and data, as described in Ref. [57]. The efficiency is calculated as the ratio of events with fewer than 20 SPD hits to the total number of events. This is obtained by integrating the SPD hit distribution up to 20 hits and dividing by the integral over all events, yielding the probability for an event to pass the SPD hit cut.

When the criterion of no additional VELO tracks is applied, not only background events are removed but also a fraction of the signal is lost. The efficiency accounts for this loss. It is calculated by selecting events with exactly four tracks originating from the same production vertex, and these particles must pass through the entire tracking system (VELO + TT + T stations). Due to ghost tracks and interactions with detector material, approximately 3% of events have more than four reconstructed tracks. Therefore, the efficiency is defined as the fraction of events that have exactly four VELO tracks reconstructed.

The reconstruction efficiency is calculated using the $J/\psi\phi$ sample shown in section 4.4. It is computed as the fraction of particles reconstructed as long tracks over the total number of charged particles produced within the LHCb angular acceptance ($2.0 < \eta < 5.0$). The reconstruction efficiency is assumed to be factorized for each particle and depends on the variables η and p_T

$$\epsilon_{rec}^{(K)}(p_T^{K^+}, p_T^{K^-}, \eta^{K^+}, \eta^{K^-}) = \epsilon_{rec}^{(K^-)}(p_T^{K^-}, \eta^{K^-}) \times \epsilon_{rec}^{(K^+)}(p_T^{K^+}, \eta^{K^+}) \tag{4.22}$$

$$\epsilon_{rec}^{(\mu)}(p_T^{\mu^+}, p_T^{\mu^-}, \eta^{\mu^+}, \eta^{\mu^-}) = \epsilon_{rec}^{(\mu^-)}(p_T^{\mu^-}, \eta^{\mu^-}) \times \epsilon_{rec}^{(\mu^+)}(p_T^{\mu^+}, \eta^{\mu^+}) \tag{4.23}$$

such that $\epsilon_{rec}^{(K^-)}$, $\epsilon_{rec}^{(K^+)}$, $\epsilon_{rec}^{(\mu^-)}$, and $\epsilon_{rec}^{(\mu^+)}$ represent the reconstruction efficiencies per track. Therefore, the total reconstruction efficiency is given by:

$$\epsilon_{rec} = \epsilon_{rec}^{(K)} \times \epsilon_{rec}^{(\mu)} \tag{4.24}$$

The muon chamber acceptance is computed as the fraction of tracks that cross the muon chambers over the number of muons reconstructed as long tracks within the fiducial region ($2.0 < \eta < 5.0$). It is assumed that the muon chamber acceptance is factorized for each muon candidate

$$\epsilon_{muAcc} = \epsilon_{muAcc}^{(\mu)}(p_T^{\mu^-}, \eta^{\mu^-}) \times \epsilon_{muAcc}^{(\mu)}(p_T^{\mu^+}, , \eta^{\mu^+}) \tag{4.25}$$

in this expression, $\epsilon_{muAcc}(p_T, \eta)$ represents the muon chamber acceptance for a single muon, which depends on p_T and η.

The muon PID efficiency is calculated as the ratio between the number of muons reconstructed as long tracks and identified by the muon chambers, and the number of muons reconstructed as long tracks within the muon chamber acceptance. Once again, the efficiency is assumed to be factorized

$$\epsilon_{muonID} = \epsilon_{muonID}^{\mu}(p_T^{\mu^-}, \eta^{\mu^-}) \times \epsilon_{muonID}^{\mu}(p_T^{\mu^+}, \eta^{\mu^+}) \tag{4.26}$$

such that $\epsilon_{muonID}^{\mu}(p_T, \eta)$ represents the muon ID efficiency for a single muon. A sample of low-multiplicity $J/\psi \to \mu^+\mu^-$ events [15] was used to study the IsMuon efficiency.

The IsMuon efficiency is computed using the Tag&Probe method [15] to obtain $N_{passed}(p_T, \eta)$, the number of muons recognized by the muon chambers, and $N_{failed}(p_T, \eta)$, the number of muons not recognized. Thus, the efficiency for each bin is estimated as:

$$\epsilon_{muonID}^{\mu}(p_T, \eta) = \frac{N_{passed}(p_T, \eta)}{N_{passed}(p_T, \eta) + N_{failed}(p_T, \eta)} \tag{4.27}$$

The muon trigger efficiency is computed as the ratio of the number of muon long tracks with a positive IsMuon identification that fire the trigger to the total number of muon long tracks with positive IsMuon in the sample. Since both muons must be correctly identified or at least one must fire the trigger for the event to be selected, the efficiency of the complete event is not simply the individual efficiency of each muon but rather a combination of the efficiencies of both muons.

$$\epsilon_{trig} = 1 - [1 - \epsilon^{\mu}_{trig}(p_T^{\mu^-}, \eta^{\mu^-})] \times [1 - \epsilon^{\mu}_{trig}(p_T^{\mu^+}, \eta^{\mu^+})] \tag{4.28}$$

where $\epsilon_{trig}(p_T, \eta)$ denotes the trigger efficiency for a single muon. The same data sample used for the IsMuon efficiency is employed again. The Tag&Probe method is also applied, with a few modifications, yielding:

$$\epsilon^{\mu}_{trig}(p_T, \eta) = \frac{N_{passed}(p_T, \eta)}{N_{passed}(p_T, \eta) + N_{failed}(p_T, \eta)} \tag{4.29}$$

with $N_{passed}(p_T, \eta)$ being the number of muons that fired the trigger, and $N_{failed}(p_T, \eta)$ the number of muons that did not fire the trigger.

The kaon PID efficiency is determined by the fraction of kaon long tracks identified by the PIDK criterion over the total number of kaon long tracks. Considering that both kaons must satisfy $PIDK > 0$, the event kaon PID efficiency is factorized as:

$$\epsilon_{kaonID} = \epsilon^{K}_{kaonID}(p_T^{K^-}, \eta^{K^-}) \times \epsilon^{K}_{kaonID}(p_T^{K^+}, \eta^{K^+}) \tag{4.30}$$

such that $\epsilon^{K}_{kaonID}(p_T, \eta)$ denotes the kaon ID efficiency for a single kaon. The kaon identification efficiency was calculated using a sample of low-multiplicity $\phi \to K^+K^-$ events. The same Tag&Probe method employed for the IsMuon efficiency is used here, but in this case, it is applied to kaons

$$\epsilon^{K}_{kaonID}(p_T, \eta) = \frac{N_{passed}(p_T, \eta)}{N_{passed}(p_T, \eta) + N_{failed}(p_T, \eta)} \tag{4.31}$$

the $N_{passed}(p_T, \eta)$ corresponds to the number of kaons correctly identified by the $PIDK > 0$ criterion, while $N_{failed}(p_T, \eta)$ represents the number of kaons that were misidentified (missed kaons).

To calculate the mass window requirement efficiency, it is necessary to account for events that fall outside the dimuon mass window (3566–3806 MeV/c^2) and dikaon mass window (1005–1035 MeV/c^2) to estimate the fraction of $\psi(2S)(\rightarrow \mu^+\mu^-)\phi(\rightarrow K^+K^-)$ events not contained within these windows. The fit described in Section 4.7 is used to compute this efficiency by taking N_{sel}, the fit integral over the selection range, and N_{total}, the fit integral over the extended mass range ($1500 < M_{\mu\mu}/(\mathrm{MeV}/c^2) < 4500$ and $990 < M_{KK}/(\mathrm{MeV}/c^2) < 1190$ MeV). The efficiency is then estimated as the ratio N_{sel}/N_{total}.

The total efficiency is used to correct the signal distributions. This correction is applied by assigning a weight w to each event, where w is the inverse of the efficiency ϵ.

4.9 Results

When the selection criteria were applied in Sec. 4.6, 40 $\psi(2S)\phi$ candidates were selected. The sample purity was found to be $p = (79.72 \pm 3.54)\%$, and the effective single-interaction integrated luminosity is $\mathcal{L}_{int}^{eff(corr)} = (1.73 \pm 0.05)$ fb^{-1}.

4.9.1 Cross-check of $J/\psi\phi$ and $\psi(2S)\phi$ cross-section

Using the same methods employed in Ref. [15], and the same dataset with an integrated luminosity of 1.73 fb^{-1}, the same selection cuts were applied: $p_T > 200$ MeV, pseudorapidity $2 < \eta < 5$ for each muon and kaon, and a veto on $m(J/\psi\phi) <$ 6000 MeV/c^2. With these considerations, it is possible to reproduce the same result and calculate the cross-section of $J/\psi(\rightarrow \mu^+\mu^-)\phi(\rightarrow K^+K^-)$, as a way to validate that the methods were correctly applied. The cross-section value for $J/\psi\phi$ under these same conditions is found to be

$$\sigma_{J/\psi\phi} = 2.51 \pm 0.08 \text{ (stat.)} \pm 0.12 \text{ (syst.)} \pm 0.05 \text{ (lumi.) pb.} \tag{4.32}$$

This result is consistent with Ref. [58], and the same efficiencies (see Tab. 4.4) were reproduced (see Tab. 4.5), indicating that the techniques are valid and can be used to determine the cross-section of $\psi(2S)\phi$.

Source	Efficiency (%)
SPD ($\epsilon_{(SPD)}$)	86.2 ± 1.3
VELO ($\epsilon_{(VELO)}$)	97.25 ± 0.05
K Reconstruction ($\epsilon_{reco}^{(K)}$)	44.2 ± 1.3
Mu Reconstruction/acceptance	77.53 ± 0.08
Muon ID (ϵ_{muAcc})	95.93 ± 0.10
Trigger (ϵ_{trig})	88.693 ± 0.030
Kaon ID (ϵ_{kaonID})	95.19 ± 0.14
Mass cut (ϵ_{mass})	88.31 ± 0.04

Table 4.4: The average efficiencies per event for the $J/\psi\phi$ data sample in [59]. Although this ANA note is only accessible to the LHCb collaboration, we decided to include it in the dissertation for bookkeeping purposes.

Source	Efficiency (%)
SPD ($\epsilon_{(SPD)}$)	86.2 ± 1.3
VELO ($\epsilon_{(VELO)}$)	97.25 ± 0.05
K Reconstruction ($\epsilon_{reco}^{(K)}$)	44.2 ± 0.1
Mu Reconstruction/acceptance	77.53 ± 0.08
Muon ID (ϵ_{muAcc})	95.93 ± 0.10
Trigger (ϵ_{trig})	88.693 ± 0.030
Kaon ID (ϵ_{kaonID})	95.19 ± 0.14
Mass cut (ϵ_{mass})	88.31 ± 0.04

Table 4.5: The average efficiencies per event for the $J/\psi\phi$ data sample were reobtained using the same methods as in [58].

Source	Efficiency (%)
SPD ($\epsilon_{(SPD)}$)	86.2 ± 1.3
VELO ($\epsilon_{(VELO)}$)	97.25 ± 0.05
K Reconstruction	46.0 ± 0.1
Mu Reconstruction/acceptance	84.78 ± 0.10
Muon ID (ϵ_{muAcc})	96.04 ± 0.16
Trigger (ϵ_{trig})	92.022 ± 0.082
Kaon ID (ϵ_{kaonID})	96.31 ± 0.15
Mass cut (ϵ_{mass})	88.91 ± 0.01

Table 4.6: Average efficiencies per event for $\psi(2S)\phi$ data sample.

The cross-section for the $\psi(2S)\phi$ pair is found to be

$$\sigma_{\psi(2S)\phi} = 0.0723 \pm 0.0117 \text{ (stat.) pb.} \tag{4.33}$$

The efficiencies were calculated using the method described in Ref. [15]. The first step involved recalculating the $J/\psi\phi$ efficiencies to perform a cross-check with the results in Ref. [15], ensuring that the procedure was functioning correctly. Subsequently, the $\psi(2S)\phi$ efficiencies were determined. The results are presented in Table 4.6.

4.9.2 Cross-section ratio

The cross-section ratio between $\psi(2S)\phi$ and $J/\psi\phi$ will be calculated in order to compare it with the result of Ref. [60], and to analyze whether there is any correlation with the cross-section ratio of $\psi(2S)$ to J/ψ. The value of the cross-section ratio between $\psi(2S)\phi$ and $J/\psi\phi$ is

$$\frac{\sigma_{\psi(2S)\phi}}{\sigma_{J\psi/\phi}} = 0.030 \pm 0.005 \text{ (stat.)} \tag{4.34}$$

where the statistical uncertainty is calculated because the samples are uncorrelated; the systematic uncertainty was not calculated because it involves correlated components; and the luminosity uncertainty cancels out because the luminosity uncertainties are fully correlated.

The ratio $\frac{\sigma_{\psi(2S)\phi}}{\sigma_{J/\psi\phi}}$ is significantly lower than the value

$$\frac{\sigma_{\psi(2S)}}{\sigma_{J/\psi}} = 0.1763 \pm 0.0029 \text{ (stat.)} \pm 0.0008 \text{ (syst.)} \pm 0.0039 \text{ (lumi.)}, \tag{4.35}$$

reported in the Ref. [60]. The discrepancy between the values may arise from the mass difference between the two final states, since diffractive processes are suppressed for higher masses.

Chapter 5

Contributions to the LHCb

One of the event generators used by LHCb is StarLight [61], a Monte Carlo event generator designed to model ultra-peripheral collisions (UPCs) and photon-induced interactions in hadronic colliders. Initially, StarLight was developed for heavy-ion physics, simulating processes where electromagnetic interactions dominate and hadronic interactions are suppressed. In these interactions, the intense electromagnetic fields of highly charged ions or protons act as sources of quasi-real photons, enabling photon-photon and photon-hadron interactions at high energies.

StarLight has the advantage of being able to simulate exclusive vector meson production. In this process, a photon emitted by one of the hadrons interacts with another hadron, resulting in the exclusive production of a vector meson, while the hadrons remain intact or dissociate into very low-mass systems. These types of processes are important for probing the gluon distribution in hadrons at small Bjorken-x values, which is the region where gluon saturation effects may start to become significant.

Although StarLight was originally designed for heavy-ion collisions, its flexibility allows it to be applied to proton-proton (pp) collisions, enabling the study of diffractive processes such as CEP. In CEP, the central system - in this dissertation, the $\psi(2S)\phi$ meson pair - is produced via colorless exchanges (photons or pomerons), with the requirement of two large rapidity gaps. This results in a clean environment to study the signal signature, as there is minimal hadronic activity in the detector.

The idea is to to compare theoretical predictions with experimental data, estimate acceptances, and validate event selection criteria in analyses involving diffractive or photon-induced processes. Furthermore, StarLight can be extended to model rare processes, such as the associated production of $\psi(2S)\phi$ mesons, assisting in the search for new phenomena and in testing QCD in the non-perturbative regime.

During my master's program, I had the opportunity to work for two months onsite at the LHC. I worked under the supervision of Gloria Corti to integrate the StarLight generator into the upgraded GAUSS framework [62].

There is more than one version of StarLight implementation in GAUSS, such as Sim09 (designed for Run 2), Sim10 (designed for Run 3), and Sim11 (designed for Run 3 and Run 4). The last one is an upgraded version for Run 3. In my work, I used Sim10. It was necessary to adapt Sim09 to Sim10 because of a change in how Gauss reads other event generators, which caused StarLight to stop working. This made it necessary to migrate StarLight from Sim09 to Sim10.

When employing the more recent Sim10-v1 simulation cycle, a significant computational improvement was achieved. Specifically, the simulation time was reduced by a factor of two compared to the Sim09 cycle, for both Run 2 and Run 3 detector configurations and conditions [63]. I continued a project that had previously started to implement StarLight for the Run 2 version of Gauss.

The native version of STARlight refers to the direct execution of the standalone C++ code, available from the official website or repository, without integration into simulation frameworks such as GAUSS (LHCb), CMSSW (CMS), or Athena (ATLAS). This approach offers greater flexibility for parameter tuning and rapid testing, while avoiding the additional computational overhead of full framework integration. In order to cross-check the Sim10 StarLight implementation, a native version was used to generate distributions for comparison.

The combined analysis of invariant mass, rapidity, and the pseudorapidities of decay products provides a comprehensive understanding of particle production and decay kinematics. The invariant mass distribution enables clear identification of resonant states, separating signal from background. Rapidity offers information about the longitudinal momentum and spatial distribution of the particle within the collision frame. Meanwhile, the pseudorapidities of the decay products characterize their angular distribution relative to the detector acceptance, which is essential for studying detector efficiency and possible asymmetries. Together, these variables allow for detailed investigations of production mechanisms, polarization effects, and effective background suppression, improving the overall precision of the analysis.

In Figs. 5.1 and 5.2, we compare the distributions for UPC production of ρ and J/ψ mesons in PbPb collisions at $\sqrt{s} = 5.02$ TeV. There is a slight deviation in mass, which does not appear in rapidity due to the symmetry. In Figs. 5.3 and 5.4, we compare the distributions for UPC production of ρ and J/ψ mesons in pPb collisions at $\sqrt{s} = 8.16$ TeV. Now it is possible to observe a slight deviation in rapidity due to the asymmetry. In Figs. 5.5 and 5.6, we compare the distributions for UPC production of ρ and J/ψ mesons in Pbp collisions at $\sqrt{s} = 8.16$ TeV, where the slight deviation in rapidity due to the asymmetry is also visible. One can see that the Gauss StarLight implementation of Sim10 shows similar distributions to the native version. A small discrepancy in the mass distribution of the resonances is reflected in the pseudorapidity distribution and requires further investigation for the impact of these differences in the future data analysis.

In conclusion, the implementation of StarLight on the upgraded simulation cycle Sim10 at LHCb was successfull for pPb, Pbp and PbPb collisions. As a next step, one needs to work on the implementation for fixed-target mode since it requires different beam settings conditions which are not working for the current implementation.

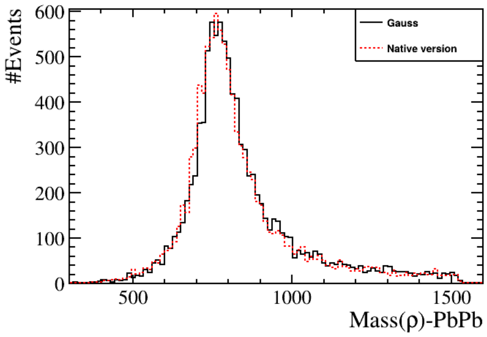

(a) Mass distribution of the ρ mesons produced in StarLight simulation of PbPb collisions.

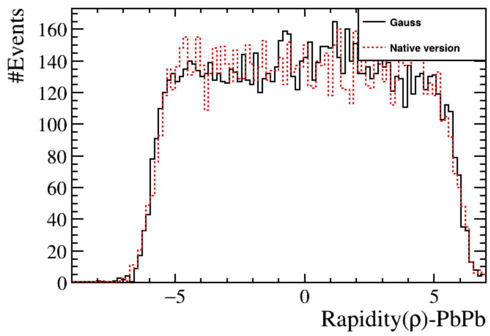

(b) Rapidity distribution of the ρ mesons produced in StarLight simulation of PbPb collisions.

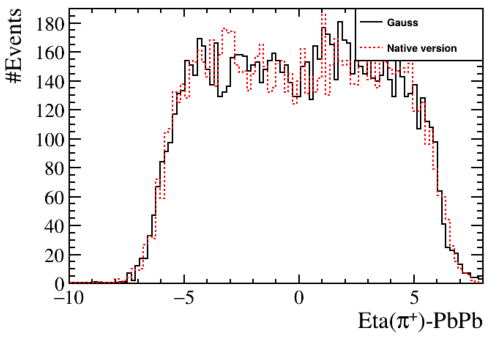

(c) Pseudorapidity distribution of the π^+ mesons produced in StarLight simulation of ρ production in PbPb collisions.

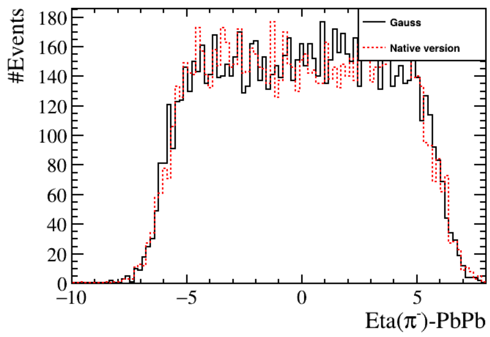

(d) Pseudorapidity distribution of the π^- mesons produced in StarLight simulation of ρ production in PbPb collisions.

Figure 5.1: Simulation of ρ production in PbPb collisions using StarLight, compared with the native version. The black line represents the STARlight simulation within the Gauss framework, while the red line corresponds to the native version.

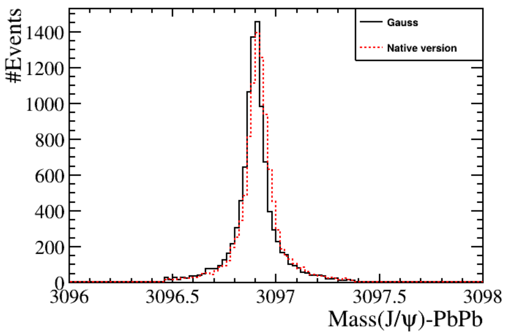

(a) Mass distribution of the J/ψ mesons produced in StarLight simulation of PbPb collisions.

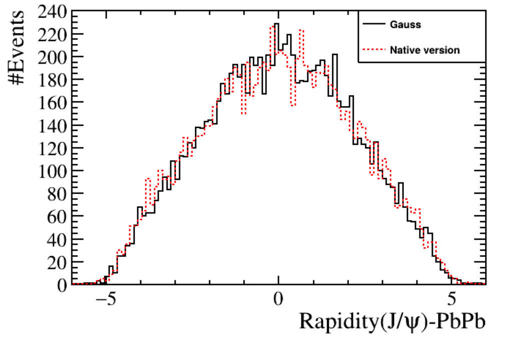

(b) Rapidity distribution of the J/ψ mesons produced in StarLight simulation of PbPb collisions.

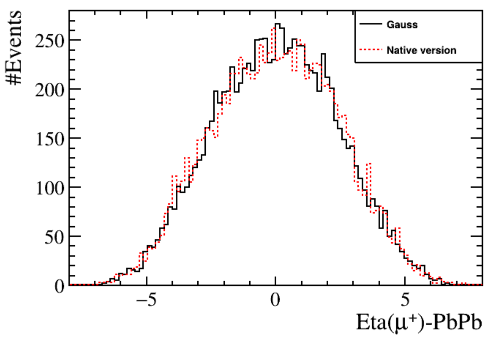

(c) Pseudorapidity distribution of the μ^+ mesons produced in StarLight simulation of J/ψ production in PbPb collisions.

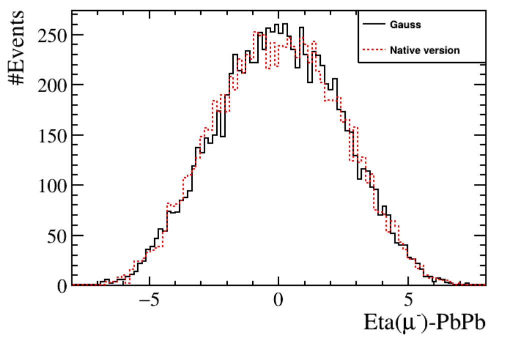

(d) Pseudorapidity distribution of the μ^- mesons produced in StarLight simulation of J/ψ production in PbPb collisions.

Figure 5.2: Simulation of J/ψ production in PbPb collisions using StarLight, compared with the native version. The black line represents the STARlight simulation within the Gauss framework, while the red line corresponds to the native version.

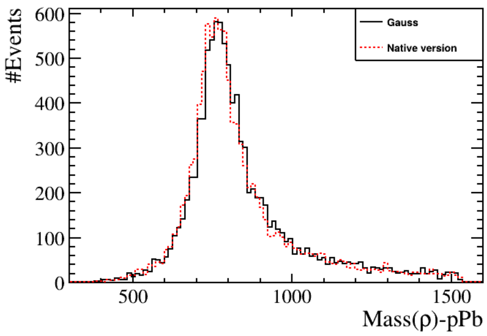

(a) Mass distribution of the ρ mesons produced in StarLight simulation of pPb collisions.

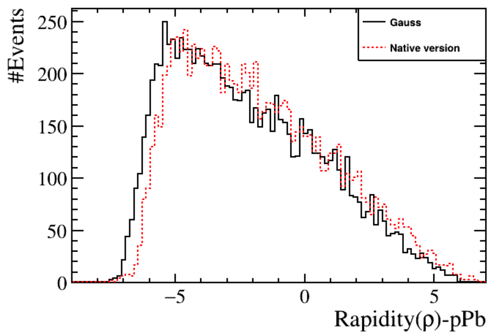

(b) Rapidity distribution of the ρ mesons produced in StarLight simulation of pPb collisions.

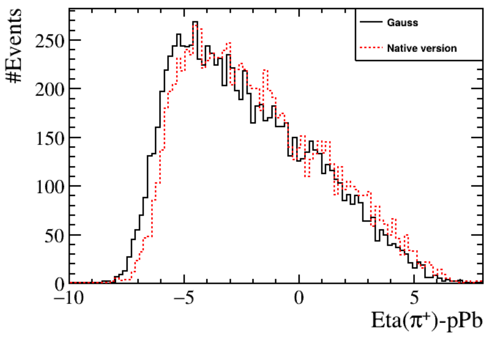

(c) Pseudorapidity distribution of the π^+ mesons produced in StarLight simulation of ρ production in pPb collisions.

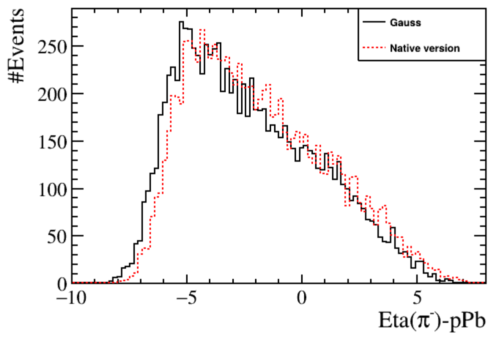

(d) Pseudorapidity distribution of the π^- mesons produced in StarLight simulation of ρ production in pPb collisions.

Figure 5.3: Simulation of ρ production in pPb collisions using StarLight, compared with the native version. The black line represents the STARlight simulation within the Gauss framework, while the red line corresponds to the native version.

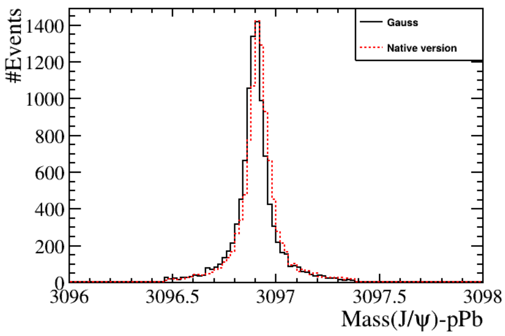

(a) Mass distribution of the J/ψ mesons produced in StarLight simulation of pPb collisions.

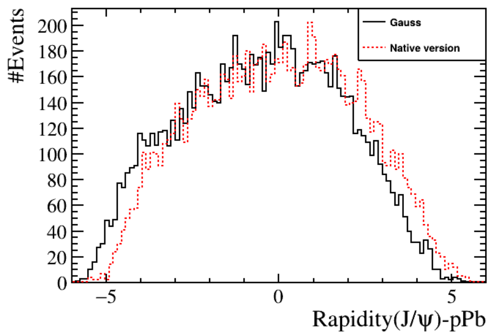

(b) Rapidity distribution of the J/ψ mesons produced in StarLight simulation of pPb collisions.

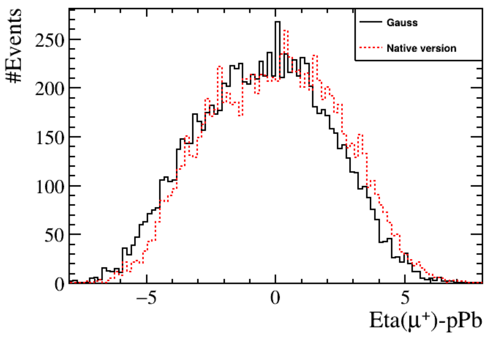

(c) Pseudorapidity distribution of the μ^+ mesons produced in StarLight simulation of J/ψ production in pPb collisions.

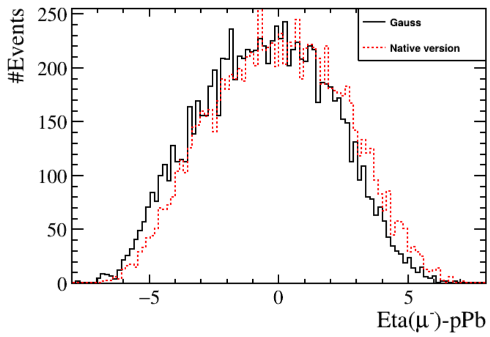

(d) Pseudorapidity distribution of the μ^- mesons produced in StarLight simulation of J/ψ production in pPb collisions.

Figure 5.4: Simulation of J/ψ production in pPb collisions using StarLight, compared with the native version. The black line represents the STARlight simulation within the Gauss framework, while the red line corresponds to the native version.

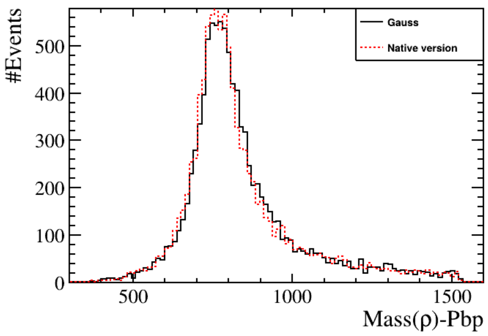

(a) Mass distribution of the ρ mesons produced in StarLight simulation of Pbp collisions.

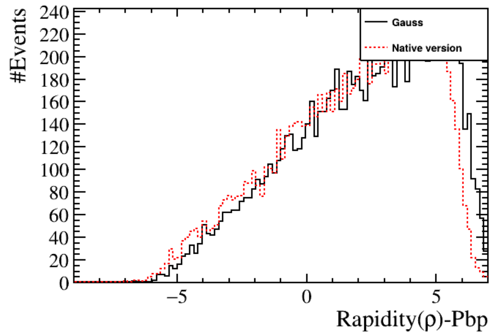

(b) Rapidity distribution of the ρ mesons produced in StarLight simulation of Pbp collisions.

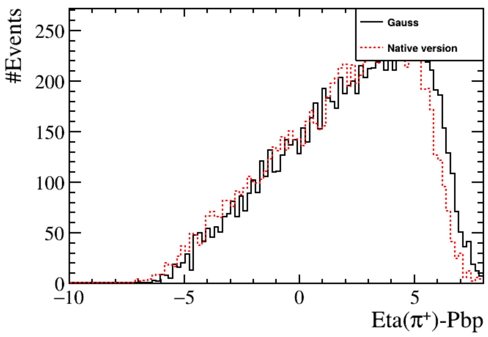

(c) Pseudorapidity distribution of the π^+ mesons produced in StarLight simulation of ρ production in Pbp collisions.

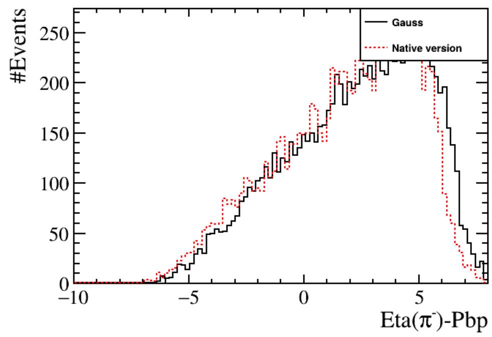

(d) Pseudorapidity distribution of the π^- mesons produced in StarLight simulation of ρ production in Pbp collisions.

Figure 5.5: Simulation of ρ production in Pbp collisions using StarLight, compared with the native version. The black line represents the STARlight simulation within the Gauss framework, while the red line corresponds to the native version.

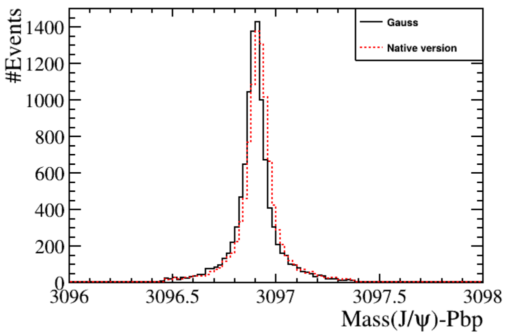

(a) Mass distribution of the J/ψ mesons produced in StarLight simulation of Pbp collisions.

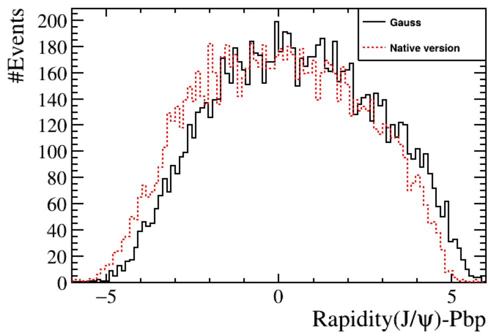

(b) Rapidity distribution of the J/ψ mesons produced in StarLight simulation of Pbp collisions.

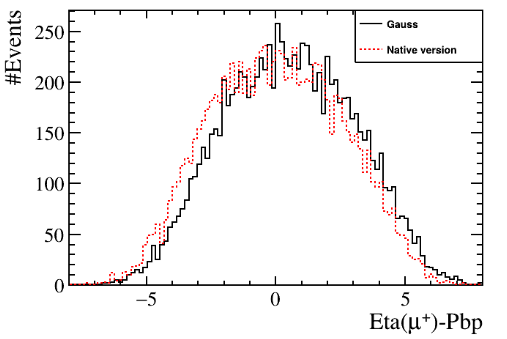

(c) Pseudorapidity distribution of the μ^+ mesons produced in StarLight simulation of J/ψ production in Pbp collisions.

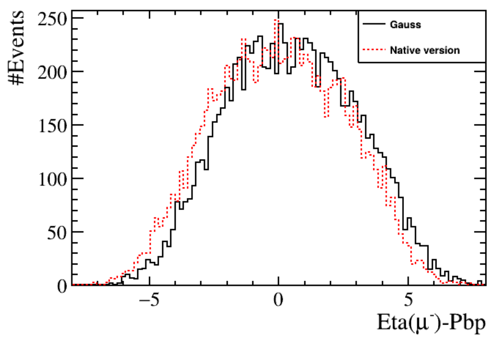

(d) Pseudorapidity distribution of the μ^- mesons produced in StarLight simulation of J/ψ production in Pbp collisions.

Figure 5.6: Simulation of J/ψ production in Pbp collisions using StarLight, compared with the native version. The black line represents the STARlight simulation within the Gauss framework, while the red line corresponds to the native version.

Chapter 6

Conclusion

This dissertation presents the first study on the production of vector meson pairs $\psi(2S)\phi$ in diffractive events in the LHCb experiment. After applying the trigger requirements in Section 4.6, 40 $\psi(2S)\phi$ candidates were selected within a pseudorapidity range of $2 < \eta < 5$ and transverse momentum $p_T > 200$ MeV for each of the four final-state particles, corresponding to an integrated luminosity of $(1747 \pm 34.94)\ \text{pb}^{-1}$. This yields a cross-section of $\sigma_{\psi(2S)\phi} = 0.0723 \pm 0.0117\ \text{pb}^{-1}$. The ratio between the $\psi(2S)\phi$ and $J/\psi\phi$ cross-sections was found to be $\frac{\sigma_{\psi(2S)\phi}}{\sigma_{J/\psi\phi}} = 0.030 \pm 0.005$.

The ratio $\frac{\sigma_{\psi(2S)\phi}}{\sigma_{J/\psi\phi}}$ was compared with the ratio $\frac{\sigma_{\psi(2S)}}{\sigma_{J/\psi}}$ reported in Ref. [60], and a slight discrepancy between the values was observed. The discrepancy between the values may be attributed to the mass difference between the two final states, as diffractive processes tend to be suppressed for heavier masses.

In addition, the implementation of STARlight in the upgraded Sim10 simulation cycle at LHCb was performed successfully for pPb, Pbp, and PbPb collisions. The next step involves working on the implementation for the fixed-target mode, as it requires different beam setting conditions that are not compatible with the current implementation.

Bibliography

[1] Spencer R. Klein et al. "STARlight: A Monte Carlo simulation program for ultra-peripheral collisions of relativistic ions". In: *Computer Physics Communications* 212 (Mar. 2017), pp. 258–268. ISSN: 0010-4655. DOI: 10.1016/j.cpc.2016.10.016. URL: http://dx.doi.org/10.1016/j.cpc.2016.10.016.

[2] Matthew Robinson. *Symmetry and the Standard Model*. Springer, 2011. URL: https://link.springer.com/book/10.1007/978-1-4419-8267-4#bibliographic-information.

[3] V. Barone and E. Predazzi. *High-Energy Particle Diffraction*. 1st ed. Theoretical and Mathematical Physics. Berlin, Heidelberg: Springer, 2002. URL: https://link.springer.com/book/10.1007/978-3-662-04724-8.

[4] Yan-Rui Liu et al. "Pentaquark and Tetraquark States". In: *Progress in Particle and Nuclear Physics* 107 (July 2019), pp. 237–320. ISSN: 0146-6410. DOI: 10.1016/j.ppnp.2019.04.003. URL: http://dx.doi.org/10.1016/j.ppnp.2019.04.003.

[5] Hua-Xing Chen et al. "An updated review of the new hadron states". In: *Reports on Progress in Physics* 86.2 (Dec. 2022), p. 026201. ISSN: 1361-6633. DOI: 10.1088/1361-6633/aca3b6. URL: http://dx.doi.org/10.1088/1361-6633/aca3b6.

[6] Prof Mark Thomson. *Handout 8 : Quantum Chromodynamics*. https://www.hep.phy.cam.ac.uk/~thomson/partIIIparticles/handouts/Handout_8_2011.pdf. Accessed: 2025-09-23.

[7] István Szanyi et al. "Pomeron/glueball and odderon/oddball trajectories". In: *Nuclear Physics A* 998 (2020), p. 121728. DOI: 10.1016/j.nuclphysa.2019.121728. arXiv: 1910.02494 [hep-ph]. URL: https://arxiv.org/pdf/1910.02494.

[8] Mark Thomson. *Modern Particle Physics*. Cambridge, UK: Cambridge University Press, 2013.

[9] Michael E Peskin and Daniel V Schroeder. *An Introduction to Quantum Field Theory*. Westview Press, 1995.

[10] Wolfgang Ochs. "The status of glueballs". In: *Journal of Physics G: Nuclear and Particle Physics* 40.4 (Feb. 2013), p. 043001. ISSN: 1361-6471. DOI: 10.1088/0954-3899/40/4/043001. URL: http://dx.doi.org/10.1088/0954-3899/40/4/043001.

[11] Y. Chen et al. "Glueball spectrum and matrix elements on anisotropic lattices". In: *Physical Review D* 73.1 (Jan. 2006). ISSN: 1550-2368. DOI: 10.1103/physrevd.73.014516. URL: http://dx.doi.org/10.1103/PhysRevD.73.014516.

[12] Colin J. Morningstar and Mike Peardon. "Glueball spectrum from an anisotropic lattice study". In: *Physical Review D* 60.3 (July 1999). ISSN: 1089-4918. DOI: 10.1103/physrevd.60.034509. URL: http://dx.doi.org/10.1103/PhysRevD.60.034509.

[13] Lorenzo Sestini. "Electroweak boson production at LHCb". In: *PoS* EPS-HEP2017 (2018), p. 402. DOI: 10.22323/1.314.0402. URL: https://cds.cern.ch/record/2302042.

[14] Barak Raimond Gruberg Cazón. *Central exclusive production of χ_c mesons in $\sqrt{s} = 13$ TeV proton-proton collisions.* Nov. 2021.

[15] Lucas Meyer Garcia. "Direct production of $J/\psi\phi$ vector mesons at the LHCb experiment without additional activity". Presented 30 Aug 2023. Universidade Federal Do Rio De Janeiro, Instituto De Fisica, 2023. URL: https://cds.cern.ch/record/2874934.

[16] V. P. Goncalves, B. D. Moreira, and F. S. Navarra. "Double vector meson production in photon–hadron interactions at hadronic colliders". In: *Eur. Phys. J. C* 76.7 (2016), p. 388. DOI: 10.1140/epjc/s10052-016-4239-x. arXiv: 1605.05840 [hep-ph].

[17] Lyndon Evans and Philip Bryant. "LHC Machine". In: *Journal of Instrumentation* 3.08 (Aug. 2008), S08001. DOI: 10.1088/1748-0221/3/08/S08001. URL: https://dx.doi.org/10.1088/1748-0221/3/08/S08001.

[18] J. Albrecht et al. "Summary of the trigger systems of the Large Hadron Collider experiments ALICE, ATLAS, CMS and LHCb". In: *Journal of Physics G: Nuclear and Particle Physics* 52.3 (2025), p. 030501. DOI: 10.1088/1361-6471/adaadc. arXiv: 2408.03881. URL: https://arxiv.org/abs/2408.03881.

[19] CERN. *The CERN Accelerator Complex.* https://home.cern/science/accelerators/accelerator-complex. Accessed: 2025-08-11.

[20] Alessandra Lombardi. "LINAC4 Commissioning". In: (2018), TH1P01. DOI: 10.18429/JACoW-LINAC2018-TH1P01. URL: https://cds.cern.ch/record/2669232.

[21] Oliver Sim Brüning et al. *LHC Design Report.* CERN Yellow Reports: Monographs. Geneva: CERN, 2004. DOI: 10.5170/CERN-2004-003-V-1. URL: https://cds.cern.ch/record/782076.

[22] Jean-Luc Caron. "CERN Accelerator Complex (operating and approved projets).. Chaine des accelerateurs du CERN (en fonctionnement et avec les projets aprouves)." AC Collection. Legacy of AC. Pictures from 1992 to 2002. 1991. URL: https://cds.cern.ch/record/841493.

[23] A Augusto Alves et al. "The LHCb Detector at the LHC". In: *JINST* 3 (2008). Also published by CERN Geneva in 2010, S08005. DOI: 10.1088/1748-0221/3/08/S08005. URL: https://cds.cern.ch/record/1129809.

[24] R. Calabrese et al. "Performance of the LHCb RICH detectors during LHC Run 2". In: *JINST* 17.07 (2022), P07013. DOI: 10.1088/1748-0221/17/07/P07013. arXiv: 2205.13400. URL: https://cds.cern.ch/record/2811056.

[25] S Amato et al. *LHCb magnet*. Technical design report. LHCb. Geneva: CERN, 2000. DOI: 10.17181/CERN.MCVC.Q12G. URL: https://cds.cern.ch/record/424338.

[26] P R Barbosa-Marinho et al. *LHCb VELO (VErtex LOcator)*. Technical design report. LHCb. Geneva: CERN, 2001. URL: https://cds.cern.ch/record/504321.

[27] R Antunes-Nobrega et al. *LHCb reoptimized detector design and performance*. Technical design report. LHCb. Geneva: CERN, 2003. URL: https://cds.cern.ch/record/630827.

[28] P R Barbosa-Marinho et al. *LHCb inner tracker*. Technical design report. LHCb. revised version number 1 submitted on 2002-11-13 14:14:34. Geneva: CERN, 2002. URL: https://cds.cern.ch/record/582793.

[29] P R Barbosa-Marinho et al. *LHCb outer tracker*. Technical design report. LHCb. Geneva: CERN, 2001. URL: https://cds.cern.ch/record/519146.

[30] In: *Journal of Instrumentation* 9.01 (Jan. 2014), P01002–P01002. ISSN: 1748-0221. DOI: 10.1088/1748-0221/9/01/p01002. URL: http://dx.doi.org/10.1088/1748-0221/9/01/P01002.

[31] Roel Aaij et al. "Design and performance of the LHCb trigger and full real-time reconstruction in Run 2 of the LHC. Performance of the LHCb trigger and full real-time reconstruction in Run 2 of the LHC". In: *JINST* 14.04 (2019). 46 pages, 35 figures, 1 table. All figures and tables are available at https://cern.ch/lhcbproject/Publications/LHCbProjectPublic/LHCb-DP-2019-001.html, P04013. DOI: 10.1088/1748-0221/14/04/P04013. arXiv: 1812.10790. URL: https://cds.cern.ch/record/2652801.

[32] The LHCb Collaboration et al. "The LHCb Detector at the LHC". In: *Journal of Instrumentation* 3.08 (Aug. 2008), S08005. DOI: 10.1088/1748-0221/3/08/S08005. URL: https://dx.doi.org/10.1088/1748-0221/3/08/S08005.

[33] Eduardo Picatoste Olloqui and (on behalf ofthe LHCb Collaboration). "LHCb Preshower(PS) and Scintillating Pad Detector (SPD): Commissioning, calibration, and monitoring". In: *Journal of Physics: Conference Series* 160.1 (Apr. 2009), p. 012046. DOI: 10.1088/1742-6596/160/1/012046. URL: https://dx.doi.org/10.1088/1742-6596/160/1/012046.

[34] S Amato et al. *LHCb calorimeters*. Technical design report. LHCb. Geneva: CERN, 2000. URL: https://cds.cern.ch/record/494264.

[35] F Archilli et al. "Performance of the Muon Identification at LHCb". In: *Journal of Instrumentation* 8.10 (Oct. 2013), P10020–P10020. ISSN: 1748-0221. DOI: 10.1088/1748-0221/8/10/p10020. URL: http://dx.doi.org/10.1088/1748-0221/8/10/P10020.

[36] R. Aaij et al. "Design and performance of the LHCb trigger and full real-time reconstruction in Run 2 of the LHC". In: *Journal of Instrumentation* 14.04 (Apr. 2019), P04013–P04013. ISSN: 1748-0221. DOI: 10.1088/1748-0221/14/04/p04013. URL: http://dx.doi.org/10.1088/1748-0221/14/04/P04013.

[37] *LHCb collaboration. Trigger Schemes.* URL: https://lhcb.web.cern.ch/speakersbureau/html/TriggerScheme.html.

[38] R Antunes-Nobrega et al. *LHCb trigger system.* Technical design report. LHCb. revised version number 1 submitted on 2003-09-24 12:12:22. Geneva: CERN, 2003. URL: https://cds.cern.ch/record/630828.

[39] R. Aaij et al. "Tesla : an application for real-time data analysis in High Energy Physics". In: *Comput. Phys. Commun.* 208 (2016), pp. 35–42. DOI: 10.1016/j.cpc.2016.07.022. arXiv: 1604.05596. URL: https://cds.cern.ch/record/2147693.

[40] K.Carvalho Akiba et al. "The HeRSCheL detector: high-rapidity shower counters for LHCb". In: *JINST* 13.04 (2018). New version to match published text. All figures and tables, along with any supplementary material and additional information, are available at https://lhcbproject.web.cern.ch/lhcbproject/Publications/LHCbProjectPublic/LHCb-DP-2016-003.html, P04017. DOI: 10.1088/1748-0221/13/04/P04017. arXiv: 1801.04281. URL: https://cds.cern.ch/record/2300319.

[41] G. Barrand et al. "GAUDI - A software architecture and framework for building HEP data processing applications". In: *Comput. Phys. Commun.* 140 (2001), pp. 45–55. DOI: 10.1016/S0010-4655(01)00254-5.

[42] *The GAUSS Project.* URL: http://lhcbdoc.web.cern.ch/lhcbdoc/gauss/.

[43] *The BOOLE Project.* URL: http://lhcbdoc.web.cern.ch/lhcbdoc/boole/.

[44] *The BRUNEL Project.* URL: http://lhcbdoc.web.cern.ch/lhcbdoc/brunel/.

[45] *The DAVINCI Project.* URL: http://lhcbdoc.web.cern.ch/lhcbdoc/davinci/.

[46] *The LHCb data flow — LHCb Starterkit Lessons documentation.* URL: https://lhcb.github.io/starterkit-lessons/first-analysis-steps/dataflow.html.

[47] M Clemencic et al. "The LHCb Simulation Application, Gauss: Design, Evolution and Experience". In: *Journal of Physics: Conference Series* 331.3 (Dec. 2011), p. 032023. DOI: 10.1088/1742-6596/331/3/032023. URL: https://dx.doi.org/10.1088/1742-6596/331/3/032023.

[48] Torbjörn Sjöstrand, Stephen Mrenna, and Peter Skands. “A brief introduction to PYTHIA 8.1”. In: *Computer Physics Communications* 178.11 (2008), pp. 852–867. ISSN: 0010-4655. DOI: https://doi.org/10.1016/j.cpc.2008.01.036. URL: https://www.sciencedirect.com/science/article/pii/S0010465508000441.

[49] T. Pierog et al. “EPOS LHC: Test of collective hadronization with data measured at the CERN Large Hadron Collider”. In: *Phys. Rev. C* 92 (3 Sept. 2015), p. 034906. DOI: 10.1103/PhysRevC.92.034906. URL: https://link.aps.org/doi/10.1103/PhysRevC.92.034906.

[50] David J. Lange. “The EvtGen particle decay simulation package”. In: *Nuclear Instruments and Methods in Physics Research Section A: Accelerators, Spectrometers, Detectors and Associated Equipment* 462.1 (2001). BEAUTY2000, Proceedings of the 7th Int. Conf. on B-Physics at Hadron Machines, pp. 152–155. ISSN: 0168-9002. DOI: https://doi.org/10.1016/S0168-9002(01)00089-4. URL: https://www.sciencedirect.com/science/article/pii/S0168900201000894.

[51] S. Agostinelli et al. “Geant4—a simulation toolkit”. In: *Nuclear Instruments and Methods in Physics Research Section A: Accelerators, Spectrometers, Detectors and Associated Equipment* 506.3 (2003), pp. 250–303. ISSN: 0168-9002. DOI: https://doi.org/10.1016/S0168-9002(03)01368-8. URL: https://www.sciencedirect.com/science/article/pii/S0168900203013688.

[52] R. McNulty. “Results and Future Plans on Central Exclusive Production with the LHCb Detector”. In: *International Journal of Modern Physics A* 29.14 (2014), p. 1446003. DOI: 10.1142/S0217751X14460037. arXiv: 1409.8113 [hep-ex]. URL: https://arxiv.org/abs/1409.8113.

[53] Patrick Koppenburg. *Stability of μ for Run 2 CEP measurements.* Tech. rep. Geneva: CERN, 2020. URL: https://cds.cern.ch/record/2743026.

[54] L. A. Harland-Lang, V. A. Khoze, and M. G. Ryskin. “Exclusive LHC physics with heavy ions and protons: SuperChic 3”. In: *Eur. Phys. J. C* 79.1 (2019), p. 39. DOI: 10.1140/epjc/s10052-018-6530-5. arXiv: 1810.06567 [hep-ph].

[55] N Tuning. *Matching VELO tracks to L0 objects for L1.* Tech. rep. revised version number 1 submitted on 2003-09-03 17:25:39. Geneva: CERN, 2003. URL: https://cds.cern.ch/record/684452.

[56] Roel Aaij et al. “Central exclusive production of J/ψ and $\psi(2S)$ mesons in pp collisions at $\sqrt{s} = 13$ TeV”. In: *JHEP* 10 (2018), p. 167. DOI: 10.1007/JHEP10(2018)167. arXiv: 1806.04079 [hep-ex].

[57] Naomi Veronika Raab. *Exclusive production of J/ψ and ϕ mesons at the LHCb experiment.* July 2022.

[58] Roel Aaij et al. “Observation of Exotic $\mathrm{J}/\psi\phi$ Resonant Structure in Diffractive Processes in Proton-Proton Collisions”. In: *Phys. Rev. Lett.* 134.3 (2025), p. 031902. DOI: 10.1103/PhysRevLett.134.031902. arXiv: 2407.14301 [hep-ex].

[59] Lucas Meyer Garcia et al. "First study of the direct production of $J/\psi\phi$ without additional activity". In: (2022). URL: https://cds.cern.ch/record/2799452.

[60] Roel Aaij et al. "Measurement of exclusive J/ψ and $\psi(2S)$ production at $\sqrt{s} =$ 13 TeV". In: *SciPost Phys.* 18.2 (2025), p. 071. DOI: 10.21468/SciPostPhys.18.2.071. arXiv: 2409.03496 [hep-ex].

[61] Spencer R. Klein et al. "STARlight: A Monte Carlo simulation program for ultra-peripheral collisions of relativistic ions". In: *Comput. Phys. Commun.* 212 (2017), pp. 258–268. DOI: 10.1016/j.cpc.2016.10.016. arXiv: 1607.03838 [hep-ph].

[62] M. Clemencic et al. "The LHCb Simulation Application, Gauss: Design, Evolution and Experience". In: ... (2010ish). Based on the GAUDI framework and interfaces with PYTHIA, EvtGen, Geant4.

[63] Concezio Bozzi. *LHCb Computing Resources: 2024 requests*. Tech. rep. Geneva: CERN, 2023. URL: https://cds.cern.ch/record/2850601.